Chemosphere 368 (2024) 143728

Contents lists available at ScienceDirect

Chemosphere

journal homepage: www.elsevier.com/locate/chemosphere

Achieving high photocatalytic NO_x removal activity using a Bi/BiOBr/TiO_2 composite photocatalyst

Paransa Alimard [a,b,c], Chen Gong [a], Ioanna Itskou [d], Andreas Kafizas [a,c,*]

[a] Department of Chemistry, Molecular Science Research Hub, 82 Wood Lane, White City Campus, Imperial College London, London, W12 0BZ, UK
[b] Science and Solutions for a Changing Planet DTP, Grantham Institute for Climate Change and the Environment, Exhibition Road, South Kensington Campus, Imperial College London, London, SW7 2AZ, UK
[c] London Centre for Nanotechnology, South Kensington Campus, Imperial College London, London, SW7 2AZ, UK
[d] Department of Chemical Engineering, South Kensington Campus, Imperial College London, London, SW7 2AZ, UK

HIGHLIGHTS

- Range of Bi/BiOBr/P25 TiO_2 composites synthesised using solvothermal and co-precipitation methods.
- Photocatalytic conversion of NO_x gas examined in accordance with ISO protocol (22197–1:2016).
- The most active composite removed 32.8% of NO and 15.1% of NO_2 under visible light.
- The highest NO removal activity of 87.2% seen at low humidity and flow rate, and high light intensity and NO_x concentration.
- The composite was a staggered type II heterojunction, with charge transfer seen between BiOBr and P25 TiO_2 sites.

GRAPHICAL ABSTRACT

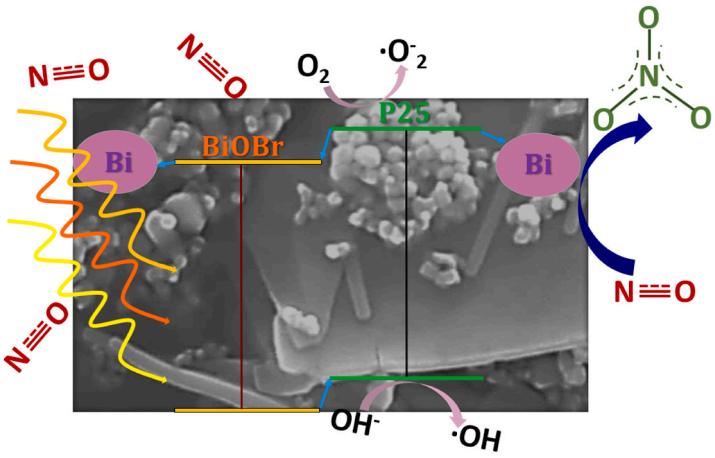

ARTICLE INFO

Handling editor: Derek Muir

Keywords:
Photocatalytic NO_x removal
Air purification
Bismuth oxybromide (BiOBr)
Titanium dioxide (TiO_2)
Composite
Surface plasmon resonance (SPR)
Charge carrier dynamics

ABSTRACT

Fossil fuel combustion generates nitrogen oxides (NO + NO_2 = NO_x), which pose threats to the environment and human health. Although commercial products containing titanium dioxide (TiO_2) can remedy NO_x pollution by photocatalysis, they only function in the ultraviolet (UV). On the other hand, bismuth oxybromide (BiOBr) is active in the visible. BiOBr is stable, affordable, and non-toxic, making it an appealing alternative. In addition, nanoparticulate Bi metal can further enhance visible light absorption through its surface plasmon properties and charge carrier lifetime by spatially separating charge. In this study, to enhance the visible-light activity of TiO_2-based photocatalysts for NO_x pollution, a composite of Bi-decorated BiOBr/TiO_2 was synthesised using a solvothermal method across varying the Ti/Bi atomic ratio (0.2, 2.2, 4.4, and 6.6), and synthesis duration (6h, 12h, and 18h). The photocatalytic performance of the synthesised composites for NO gas removal was investigated

* Corresponding author. Department of Chemistry, Molecular Science Research Hub, 82 Wood Lane, White City Campus, Imperial College London, London, W12 0BZ, UK.
E-mail address: a.kafizas@imperial.ac.uk (A. Kafizas).

https://doi.org/10.1016/j.chemosphere.2024.143728
Received 8 October 2024; Received in revised form 30 October 2024; Accepted 9 November 2024
Available online 21 November 2024

using an adapted ISO method (22197–1:2016). Analysis showed that the preferential growth of the (010) crystal facet in BiOBr and the presence of Bi metal both play an important role in the superior photocatalytic activity seen in our Bi-decorated BiOBr/TiO_2 composite. The composites were characterised using X-ray diffraction (XRD), attenuated total reflectance - Fourier transform infrared spectroscopy (ATR-FTIR), high-resolution scanning electron microscopy (HR-SEM), UV–Vis diffuse reflectance (DRS) spectroscopy, transmission electron microscopy (TEM), scanning transmission electron microscopy (STEM), scanning electron microscopy (SEM), energy dispersive X-ray spectroscopy (EDS), X-ray photoelectron spectroscopy (XPS), Raman spectroscopy, Brunauer-Emmett-Teller (BET) analysis, thermogravimetric analysis (TGA), and diffuse reflectance transient absorption spectroscopy (DR-TAS). Our research shows that the Bi/BiOBr–TiO_2 composite synthesised through a 12h solvothermal method with a Ti/Bi atomic ratio of 4.4 exhibits the highest photocatalytic performance towards both NO and NO_2 oxidation; with 32.8% and 54.9% NO removal and 15.1% and 29.5% NO_2 under visible and UV lamps, respectively.

1. Introduction

Nitrogen oxides (NO_x) are formed when fossil fuels are combusted in air from the reaction of nitrogen (N_2) and oxygen (O_2). NO_x causes acid rain, which can negatively impact ecosystems and vegetation, potentially leading to problems such as fish mortality. Additionally, NO_x contributes to the formation of smog and ground-level ozone and is responsible for millions of deaths worldwide (Zhou et al., 2015). NO_x emissions have generally risen with increased fossil fuel use, particularly in city environments where roadside traffic is common.

The majority of NO_x pollution is released in the form of NO (Spicer et al., 1993), which can undergo conversion to NO_2 through reactions with ozone (O_3) (Yagi and Tanaka, 1979). Moreover, the photolysis of O_3 produces peroxyl radicals ($ROO^{\bullet}$) that can facilitate the conversion of NO to NO_2 (O. World Health Organization and T. Environmental Health, 2006). Therefore, NO participates in O_3 depletion while generating more highly toxic NO_2 (**Equation (1)**).

$$NO + O_3 \rightarrow NO_2 + O_2 \qquad \text{Equation 1}$$

The recommended exposure limit (REL) for NO_2 over a short-term period is just ~100 ppb, and at 13 ppm the IDLH, immediately dangerous to life or health, is reached resulting in potentially lethal respiratory and cardiovascular conditions (Organization, 2006). The annual mean concentration of NO_2 has been regulated by the World Health Organization (WHO) with limits recently revised to ~5 ppb (Organization, 2006; UNION, 2008).

Due to the harmful impact of NO_x on health and the environment, reducing its air levels is essential. Methods to convert ambient NOx include biofiltration, wet scrubbing, selective catalytic reduction, and photocatalysis (Ângelo et al., 2013). Among these methods, photocatalysis is a green method that harvests and utilises solar energy with no extra required energy input and has attracted increasing attention.

Titanium dioxide (TiO_2) is the most popularly studied and applied photocatalyst because of its stability, low cost, and versatility in being able to drive a wide range of reactions (Ao et al., 2003). To generate electron-hole pairs in the anatase and rutile phases of TiO_2, which possess bandgaps of 3.2 eV and 3.0 eV, ultraviolet (UV) photons with wavelengths 387 nm and 413 nm are necessary, respectively. The proportion of sunlight that can be absorbed by the anatase and rutile phases in power terms is 7.32% and 10.76%, and in flux terms is just 1.53% and 2.72%, respectively (Fthenakis and Lynn, 2010). While studies into the photocatalytic activity of TiO_2 have shown that the anatase phase generally exhibits higher activity than its other phases (Mills and Le Hunte, 1997), the cost-effective commercial TiO_2 photocatalyst (P25) with a composition of roughly 80% anatase and 20% rutile tends to exhibit higher activities than anatase alone (Nargiello and Herz, 1993). Averaging its components, P25 has a bandgap of ~3.05 eV with a valence band (oxidation) potential of +2.90 V vs NHE, and the reduction potential of the conduction band (reduction) potential of −0.13 V vs NHE (Qin et al., 2020). Photo-oxidation of NO is possible over TiO_2 because the oxidation potentials of NO (+2) to HONO (+3) to NO_2 (+4), to HNO_3 (+5) are −1.04, −1.06 and −0.86 V vs NHE, respectively (Milazzo et al., 1978; Kato, 2020). Up to now, a plethora of strategies have been explored to improve the performance of TiO_2, including the use of surface co-catalysts (Zhang and Wang, 2013), heterojunctions (Li et al., 2016), metal nanoparticles (Zhong et al., 2009; Ku et al., 2008), heterogeneous composites (Zhang and Wang, 2013), carbonaceous materials (Leary and Westwood, 2011), and surface absorbates and dopants (Zhao et al., 2008; Horikoshi et al., 2011; Li et al., 2008). Among these modifications, combining TiO_2 with another semiconductor to form a heterojunction is considered one of the most promising strategies (Xu et al., 2020; Xia et al., 2022; Zhang et al., 2021).

Bismuth Oxyhalides, denoted as BiOX (where X represents Cl, Br, or I), are innovative layered materials known for their exceptional optical and electrical properties, making them suitable for a range of applications, including photocatalysis. These BiOX compounds belong to the V–VI–VII ternary semiconductors and exhibit a matlockite structure. This structure features layers of [X–Bi–O–Bi–X] held together by van der Waals forces through halogen atoms, while the atoms within each layer are covalently bonded. This unique arrangement imparts excellent electrical, optical, and mechanical properties to the material. In each [X–Bi–O–Bi–X] layer, a bismuth atom is surrounded by four oxygen and four halogen atoms, resulting in an asymmetric decahedral symmetry (Gondal et al., 2017). The open crystalline structure of BiOX, which is composed of layers of $[Bi_2O_2]^{2+}$ interspersed with a double layer of X^- ions, exhibits internal static electric fields, which are postulated to improve charge carrier separation (Wu et al., 2017). The BiOBr form has a narrower bandgap (~2.8 eV) than TiO_2, with valence and conduction bands at +2.71eV and −0.24 eV vs NHE, respectively (Wu et al., 2017). Fig. S1 shows the solar spectrum between 300 and 1000 nm at sea level and illustrates the improved light harvesting of BiOBr compared to that of TiO_2, with BiOBr being able to absorb 13.86% of the solar spectrum in power terms and 4.27% in terms of flux. These characteristics make BiOBr a strong contender for photocatalytic applications for NO_x remediation (Wu et al., 2017; Montoya-Zamora et al., 2020; Xin et al., 2023; Li et al., 2023), and a promising candidate to form heterojunctions with TiO_2 (Li et al., 2022; Meng et al., 2021; Wei et al., 2013; Tan et al., 2016; Wang et al., 2021; Juntrapirom et al., 2021; Hermawan et al., 2021; Hailili et al., 2024).

Bi metal exhibits surface plasmon resonance (SPR), which increases the visible light absorption range, increasing solar energy harvesting efficiency (Kang et al., 2015). It can also act as an electron trapping site, improving charge separation and lifetime (Singh and Karmakar, 2010/02). Bi possesses distinctive electronic characteristics, such as a large mean free path, an extended Fermi wavelength, high carrier mobilities, a low charge carrier density, and a small effective electron mass, enabling it to demonstrate stable plasmonic photocatalytic activity (Zhang et al., 2021/09). Elemental Bi has also been utilised in photocatalysis due to its photosensitization properties and narrow bandgap (Ma et al., 2012/10). It was also recently shown that Bi metal alone can drive photocatalytic NO_x removal under UV–visible light (Zhang et al., 2021/09; Dong et al., 2014).

In this study, composites made of i) Bi metal, ii) BiOBr, and iii) TiO_2

were synthesised using a simple one-step solvothermal method. Several composites were synthesised with varying atomic ratios of Ti/Bi. Our results show that such composites perform significantly better than the individual parent materials in their ability to drive photocatalytic NO_x removal under UV and visible light (300–800 nm). The mechanism for the improved photocatalytic performance was studied by investigating the band structure and charge carrier lifetime.

2. Experimental

2.1. Chemicals and materials

In this study, Potassium bromide (99%), Bismuth (III) nitrate (98%) (98%), acetic acid (99%), ethylenediaminetetraacetic acid disodium (EDTA, 99%), and ethylene glycol (99%) were obtained from Sigma-Aldrich. TiO_2 (P25) was acquired from Thermo Scientific. NO and NO_2 gases (100 ppm concentration diluted in N_2) were purchased from BOC. Ethanol absolute (99.5%) and cetyltrimethylammonium bromide (CTAB) (98%) were purchased from VWR and Tokyo Chemical Industry (TCI), respectively.

2.1.1. Bi/bismuth oxybromide synthesis using a solvothermal method

BiOBr-2h, Bi–BiOBr-4h, Bi–BiOBr-6h, Bi–BiOBr-8h, Bi–BiOBr-10h, and Bi–BiOBr (12 h) were synthesised using a reported method (Wang et al., 2020). The synthesis method can be found in the SI (S1.1).

2.1.2. Bismuth oxybromide synthesis using a co-precipitation method

BiOBr-CP was synthesised using a reported co-precipitation method (Montoya-Zamora et al., 2020). The synthesis method can be found in the SI (S1.2).

2.1.3. Bi/bismuth oxybromide/P25 composite synthesis using a solvothermal method

Initially, $Bi(NO_3)_3{\cdot}5H_2O$ was added to 17 mL of ethylene glycol and subjected to bath sonication until complete dissolution. Subsequently, CTAB was added to 18 mL of ethylene glycol and sonicated using an ultrasonic bath until it dissolved. In another breaker, P25 was dispersed in 35 mL of water magnetically. Then, the P25 mixture was added to bismuth solution dropwise (~1 drop per second), followed by the addition of CTAB solution dropwise to the former solution (~1 drop per second). Then, the mixture was sonicated using a horn sonication probe (SONICS-Vibra Cell) for 5 min (amplitude 30%, 3 s on 3 s off). The mixture was transferred to a 200 mL Teflon-lined autoclave and underwent solvothermal treatment at 180 °C for 12 h. The resulting precipitate was separated using filter paper, washed with water and ethanol, and then dried at 60 °C overnight. The final product obtained was a Bi/BiOBr/P25 composite. A series of composite Bi/BiOBr/P25 composites were synthesised with different atomic ratios of Ti/Bi (0.2, 2.2, 4.4, and 6.6). The amount of chemicals which used to prepare the composites is presented in Table 1. The composites denoted Bi–BiOBr–P 0.2, Bi–BiOB–P 2.2, Bi–BiOBr–P 4.4, and Bi–BiOBr–P 6.6, contained 0.2, 2.2, 4.4, and 6.6 of Ti/Bi in atomic ratio. Two additional Bi–BiOBr–P 4.4 composites were synthesised with the same method but various solvothermal durations (6 and 18 h) to explore the effect of reaction time on the structure and the performance (Wang et al., 2020). These composites were denoted as Bi–BiOBr–P 4.4–6h and Bi–BiOB–P 4.4–18h.

2.1.4. Bismuth oxybromide/P25 composite synthesis using a co-precipitation method

BiOBr–P 4.4-CP composite was synthesised using a reported co-precipitation method (Montoya-Zamora et al., 2020). The synthesis method can be found in the SI (S1.3).

2.1.5. Summary of all samples produced herein

All of the samples synthesised in this study are shown in Table 2.

2.2. Physical characterisation

To characterise the produced photocatalyst, various techniques were employed. X-ray diffraction (XRD) patterns were measured with a Bruker D2 Phaser diffractometer with parallel beam optics equipped with a Lynx-Eye detector. Using a Cu source (V = 30 KV, I = 10 mA) with Cu $K_{\alpha1}$ radiation ($\lambda = 1.54056$ Å) and Cu K_{a2} radiation ($\lambda = 1.54439$ Å) X-ray were generated and emitted with an intensity ratio of 2:1. Patterns were collected between $5^\circ \leq 2\Theta \leq 80^\circ$ for samples with a step size of 0.02°. The patterns were compared to standards from the Inorganic Crystal Structure Database (ICSD). Using the Debye-Scherrer equation, the primary mean crystallite size of samples was determined (Patterson, 1939) High-resolution scanning electron microscopy (HR-SEM) along with Energy Dispersive X-ray spectroscopy (EDS/EDX) to measure the elemental analysis were both conducted using a Zeiss Sigma 300 FEG SEM system. Conductive carbon adhesive tape was used for SEM images to fix the samples on SEM mountings. Raman spectroscopy was carried out at room temperature using the Bruker Senterra II Raman microscope with a 532 nm laser excitation wavelength, within 50–1000 cm^{-1} (resolution: 1.5 cm^{-1}), UV–Vis diffuse reflectance (DRS) measurements from 200 to 800 nm (resolution: 1 nm) were measured using a Shimadzu UV-2600 spectrophotometer with an integrations sphere, employing a barium sulfate powder-pressed disc as a diffuse reflectance standard. Thermogravimetric analyses (TGA) were performed using a DISCOVERY-TGA550 under air (BOC, CP grade) from 25 °C up to 900 °C (resolution: 5 °C per minute). Attenuated total reflection Fourier transform infrared (ATR-FTIR) was measured using an Agilent Cary 630 analyser from 400 to 4000 cm^{-1} (resolution: 0.2 cm^{-1}). Transmission electron microscopy (TEM) and scanning transmission electron microscopy were conducted using a JOEL JEM-2100Plus electron microscope

Table 2
The naming of all samples synthesised in this study.

Sample	Synthesis method	Synthesis duration	Atomic ratio Ti/Bi
BiOBr-CP	Co-precipitation	24h	–
BiOBr-2h	Solvothermal	2h	–
Bi–BiOBr-4h	Solvothermal	4h	–
Bi–BiOBr-6h	Solvothermal	6h	–
Bi–BiOBr-8h	Solvothermal	8h	–
Bi–BiOBr-10h	Solvothermal	10h	–
Bi–BiOBr	Solvothermal	12h	–
Bi–BiOBr–P0.2	Solvothermal	12h	0.2
Bi–BiOBr–P2.2	Solvothermal	12h	2.2
Bi–BiOBr–P4.4	Solvothermal	12h	4.4
Bi–BiOBr–P6.6	Solvothermal	12h	6.6
BiOBr–P4.4-CP	Co-precipitation	24h	4.4
Bi–BiOBr–P4.4–6h	Solvothermal	6h	4.4
Bi–BiOBr–P4.4–18h	Solvothermal	18h	4.4

Table 1
The amounts of chemicals used to prepare Bi–BiOBr–P-0.05, Bi–BiOBr–P-0.5, Bi–BiOBr–P-1, and Bi–BiOBr–P-1.5 composites.

		Sample			
		Bi–BiOBr–P 0.2	Bi–BiOBr–P 2.2	Bi–BiOBr–P 4.4	Bi–BiOBr–P 6.6
Chemical	**$Bi(NO_3)_3{\cdot}5H_2O$**	6.42 mmol (3.110 g)	4.14 mmol (2.000 g)	3 mmol (1.455 g)	2.41 mmol (1.169 g)
	CTAB	6.42 mmol (2.340 g)	4.14 mmol (1.500 g)	3 mmol (1.090 g)	2.41 mmol (0.879 g)
	P25	1.42 mmol (0.113 g)	9.2 mmol (0.735 g)	13.31 mmol (1.063 g)	15.8 mmol (1.260 g)

and a high-resolution JOEL JEM-2100F field emission electron microscope at 200 KV. A fast Fourier transform (FFT) was employed to obtain digital-selected-area electron diffraction patterns (SAEDP) from the high-resolution TEM adopting ImageJ software. X-ray photoelectron spectroscopy (XPS) measurements were conducted on a Thermo Scientific K-Alpha^{+} surface analysis X-ray photoelectron spectrophotometer with a MXR3 Al K_{α} monochromatic X-ray source. N_2 sorption isotherms were obtained at 77 K using a Micrometrics 3Flex volumetric sorption analyser. Before the measurements, the samples were degassed ex-situ using a Micrometrics VacPrep Degasser at 120 °C overnight at 2 × 10^{-5} bar, followed by in-situ degas using the 3Flex sorption analyser at 110 °C for 4 h down to 7 × 10^{-5} bar. The specific surface areas of the samples were determined using the Brunauer-Emmett-Teller (BET) method (Brunauer et al., 1938). The total pore volume (V_{tot}) was estimated from the amount of adsorbed N_2 at $P/P_0 = 0.99$. The micropore volume (V_{micro}) was calculated using the Dubinin-Radushkevich method (Dubinin, 1947), and the mesopore volume (V_{meso}) was obtained by subtracting V_{micro} from V_{total}.

2.3. Photocatalytic activity measurement

The photocatalytic NO removal experiments on the synthesised samples were conducted using a continuous flow reactor in an air pollution simulation chamber, built by the ISO (22197–1:2016). The details of photocatalytic measurements were reported in the SI (S2.1).

2.4. Transient absorption spectroscopy (TAS)

Transient absorption spectroscopy was conducted from the microsecond to second timescale in diffuse reflection mode using a Nd:YAG laser (OPOTEK Opolette 355 II, ~6 ns pulse width) as the excitation source, emitting UV light at 355 nm from the third harmonic (~220 μJ cm^{-2} per pulse, repetition rate of 0.67 Hz).

A 100 W Bentham IL1 quartz halogen lamp served as the source for generating probe light. To minimize short-wavelength irradiation from the probe lamp, long-pass filters from Comar Instruments were placed between the lamp and the sample. Transient changes in diffuse reflectance from the sample were collected with a 2″ diameter, 2” focal length lens, and directed to a monochromator (Oriel Cornerstone 130). Measurements were taken at wavelengths between 600 and 1100 nm, in 100 nm intervals.

Time-resolved changes in diffuse reflectance were detected using a Si photodiode (Hamamatsu S3071). Data for times faster than 3.6 ms were recorded with an oscilloscope (Tektronics DPO3012) via an amplifier box (Costronics), while data for times slower than 3.6 ms were recorded using a National Instrument DAQ card (NI USB-6251). Each kinetic trace was averaged over at least 100 laser pulses and measurements.

Experiments were triggered by a photodiode (Thorlabs DET10A) that responded to scattered laser light. Data acquisition and processing were managed with custom-built LabVIEW software. For each experiment, a few milligrams of the sample were pressed between two microscope slides secured with masking tape, and measurements were conducted in air. In the TAS study, prepared Bi–BiOBr–P composite samples with different Ti/Bi atomic ratios, along with Bi–BiOBr and P25 as parent materials were tested.

3. Results and discussion

3.1. Overview of the samples studied

In this study, BiOBr and Bi–BiOBr composites were synthesised over a range of time periods using a solvothermal method to investigate the impact of solvothermal time on the crystalline structure and morphology of the product. Interaction between ethylene glycol, which was used as a solvent, and Bi^{3+} cations are proposed to form $Bi(OCH_2CH_2OH)^{2+}$ alkoxides, where additionally, ethylene glycol can act as a reducing agent and drive the formation of metallic Bi (Prabhu et al., 2020). Cetrimonium bromide was employed as both a Br source and a quaternary ammonium surfactant, which can direct the formation of lamellar structures, where herein, BiOBr sheets were formed (Huo et al., 2012).

Bi–BiOBr–P composites were synthesised by employing various atomic ratios of Ti/Bi (0.2, 2.2, 4.4, and 6.6) to find the optimal ratio for high photocatalytic performance. Bi–BiOBr–P 4.4 demonstrated superior photocatalytic performance to NO photo-oxidation compared to Bi–BiOBr–P 0.2, Bi–BiOBr–P 2.2, and Bi–BiOBr–P 6.6. Subsequently, to compare the solvothermal method with a coprecipitation method that did not produce metallic Bi, and therefore, investigate the role of Bi on the photocatalytic activity, BiOBr–P with an atomic ratio of Ti/Bi of 4.4 was synthesised, and labelled Bi–BiOBr–P 4.4-CP.

In our employed solvothermal procedure, Bi metal nanoparticles were formed in the composite, which showed broad absorption across the visible range due to its localised surface plasmon resonance (LSPR). It was found that the presence of Bi metal both increased charge carrier lifetime and mitigated the production of NO_2 during the photocatalytic removal of NO gas (Sun et al., 2015).

3.2. Scanning electron microscopy (SEM)

The SEM images of the synthesised BiOBr-2h, Bi–BiOBr-4h, Bi–BiOBr-6h, Bi–BiOBr-8h, and Bi–BiOBr are shown in Fig. S2 (a, b, c, d, e, and f, respectively). The images show that BiOBr-2h, Bi–BiOBr-4h, Bi–BiOBr-6h, and Bi–BiOBr-8h are porous hierarchical microspheres composed of flakes, wherein the porosity seems to decrease as the solvothermal reaction duration increases. In Fig. S2 (e) and (f) the Bi–BiOBr (12h) flakes, forming the microspheres, adopt a more tightly packed structure, resulting in a significant reduction in porosity. In addition to spherical shapes, Bi–BiOBr particles also include cubic particles, showing a wide size distribution ranging from approximately 300 nm to 5 μm.

Fig. 1 (a) and (b) illustrate the SEM images of the Bi/BiOBr/P25 composite sample Bi–BiOBr–P 4.4, with microspheres of Bi–BiOBr were covered by P25 particles. Moreover, embedding the P25 particles among the BiOBr flakes increased the porosity of the microspheres compared to pristine Bi–BiOBr. In Fig. 1 (b), Bi–BiOBr flakes are seen to be decorated by P25 nanoparticles, with the thickness of the flakes ~10 nm. A side-on SEM image of the composite after being spray coated onto glass showed a thickness of ~9.5 μm at its thickest point (Fig. S3).

3.3. Energy dispersive X-ray spectroscopy (EDS)

Elemental analysis of Bi–BiOBr and Bi–BiOBr–P 4.4 was conducted using EDS. The results confirmed the presence of the expected elements, reported in Table 3. Theoretically, Bi–BiOBr should contain a similar level of at. % of Bi, O, and Br, respectively, however, the EDS results revealed a decrease in the at. % of O compared to Bi and Br, indicating the presence of O vacancies in the structure. The Bi–BiOBr–P 4.4 composite, based on the stoichiometric formulation, should contain 26.27, 60.54, 6.13, and 6.13 at.% of Ti, O, Bi, and Br, respectively. As depicted in Table 3, a decrease in the at.% of O alongside an increase in the at.% of the other elements was seen. The EDS spectra of Bi–BiOBr (12h) and Bi–BiOBr–P 4.4 can be observed in Fig. S4, suggesting the empirical formulae of $Bi_{1.46}OBr_{1.66}$ and $Bi_{1.12}O_{7.\ 4}BrTi_{4.96}$ for BiOBr and Bi–BiOBr–P 4.4, respectively. The expected empirical formula for the Bi–BiOBr–P 4.4 composite is $BiO_{9.8}BrTi_{4.4}$.

3.4. Transmission electron microscopy (TEM)

In Fig. S5a, the Bi–BiOBr microsphere is shown, lacking apparent surface porosity. Some flakes of Bi–BiOBr are also observable, as depicted in Fig. S5b. Within Figs. S5a and b the wide flakes exhibit partial amorphousness, likely due to the presence of oxygen vacancies, and a high concentration of Bi metal particles formed on the surface,

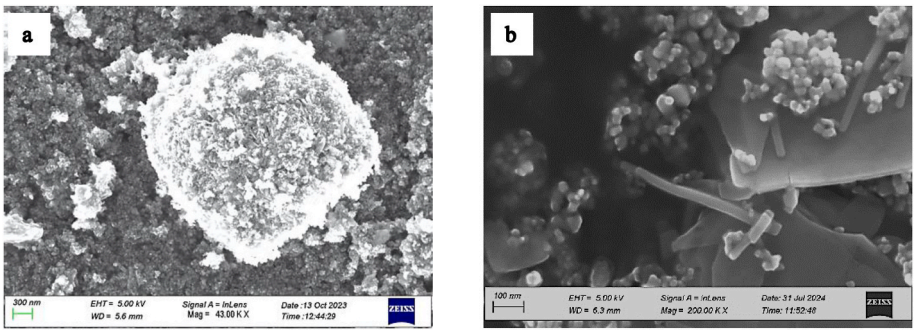

Fig. 1. SEM images of Bi–BiOBr–P 4.4, a Bi/BiOBr/P25 composite produced from a solvothermal reaction for 12 h with a Ti/Bi ratio of 4.4 at (a) 43k magnification and (b) 200k magnification.

Table 3
Energy dispersive X-ray spectroscopy (EDS) test results and empirical formula of Bi–BiOBr and Bi–BiOBr–P 4.4.

		Sample	
		Bi–BiOBr	BiOBr–P 4.4
Element (at. %)	**Bi**	35.5	7.8
	O	24.3	51.1
	Br	40.2	6.9
	Ti	–	34.2

leading to crystalline disorder. Additionally, holes can be observed in the structure of the flakes, likely caused by the demolition of the damaged and disordered crystal under high pressure in the solvothermal reactor. The holes increase the surface area and porosity of the material. Fig. S5c highlights darker dots attributed to bismuth metal detached from the crystal. Digital diffraction using a fast Fourier transform (FFT) was conducted on the entire image, encompassing all grains within the frame, as depicted in the top right of Fig. S5d. The d-spacing in this image measures 0.187 nm and 0.15 nm, corresponding to the BiOBr (104) lattice plane and Bi metal (107) lattice plane, respectively, based on XRD patterns using BiOBr-ICSD-61225 and Bi-ICSD-64703 for studying d-spacing.

Fig. 2 depicts TEM images of the Bi–BiOBr–P 4.4 composite. In Fig. 2a a wide size distribution for Bi–BiOBr flakes can be observed along with P25 nanoparticles. Fig. 2b is a focused region of Fig. 2a that shows the holes that are present in the flake structure of Bi–BiOBr. By oxygen vacancies and bismuth migration, a significant number of holes can be observed in the wide Bi–BiOBr flake in Fig. 2a and b, perhaps caused by escaping Bi atoms from the structure, resulting in the decomposition of $[Bi_2O_2]^{2+}$ slabs. In Fig. 2c, dark dots with a sharp size-distribution range of less than 10 nm approximately, spreading all over the composite, represent Bi metal which migrated after oxygen vacancies in the crystal structure (causing crystal disorder). The highlighted part of Fig. 2c was focused and studied to obtain the d-spacing of lattice planes.

The FFT was conducted on the entire image, as represented in the top right of Fig. 2d. The d-spacing in this image was measured 0.124 nm, 0.36 nm, and 0.186 nm, corresponding to the Bi (1 2 5), anatase (1 0 1), and BiOBr (1 0 4) lattice planes respectively, using Bi-ICSD-64703, anatase-ICSD-142922, and BiOBr-ICSD-61225. These results revealed that the darker particles in the image were sites where more dense bismuth metal.

3.5. X-ray diffraction (XRD)

The crystal structures of the BiOBr-2h, Bi–BiOBr-4h, Bi–BiOBr-6h, Bi–BiOBr-8h, Bi–BiOBr-10h, Bi–BiOBr (12h), and BiOBr-CP were measured using XRD, and their diffraction patterns are depicted in

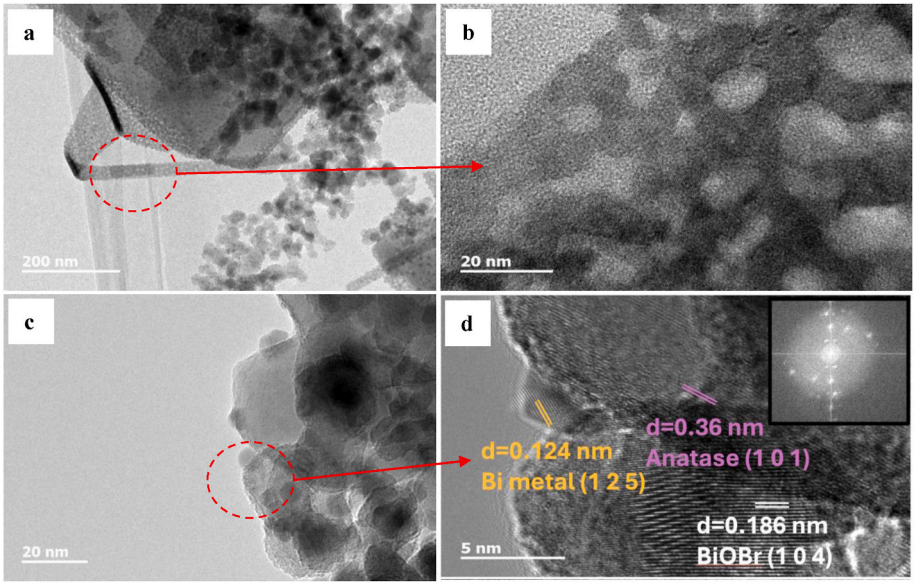

Fig. 2. High resolution TEM images of Bi–BiOBr–P 4.4, a Bi/BiOBr/P25 composite produced from a solvothermal reaction for 12 h with a Ti/Bi ratio of 4.4 at increasing magnification from (a) to (d). In (d) an insert is shown of the Fourier transform of the lattice spacing to generate an electron diffraction pattern from which d-spacings were determined, with the (104), (125) and (101) planes of the BiOBr, Bi and anatase TiO_2 phases seen, respectively.

Fig. S6. The samples conform to the anticipated tetragonal structure (BiOBr-ICSD-61225-4). The XRD patterns of Bi–BiOBr-4h, Bi–BiOBr-6h, Bi–BiOBr-8h, Bi–BiOBr-10h, and Bi–BiOBr depict an extra peak at 27.19° which corresponds to the (012) crystal plane of Bi metal (Bi-ICSD-64703). This peak confirms that Bi metal has been formed through the reduction of BiOBr during the solvothermal processes. All XRD patterns show that the most prevalent peak was the (110) reflection followed by the (102) reflection in the BiOBr phase, with a near analogous (110)/(102) peak ratio seen across all samples, indicating that the particles were dominated by the (001) crystal plane (Mi et al., 2018). BiOBr-CP also adopted the expected tetragonal structure of BiOBr, with the particles of this sample dominated by the (001) crystal plane, similar to the aforementioned samples. However, the ratio of the (110)/(102) peak was significantly larger compared to samples made by a solvothermal process.

The average crystal size can be determined using the Scherrer equation, shown below:

$$D = \frac{K\lambda}{\beta.cos\ (\theta)} \qquad \text{Equation 11}$$

where D is the average crystallite size, K is a shape constant (0.9), λ is the X-ray wavelength (0.154056 nm), β is the full width at half maximum (FWHM) and Θ is the Bragg angle. The crystallite sizes of BiOBr-2h, Bi–BiOBr-4h, Bi–BiOBr-6h, Bi–BiOBr-8h, Bi–BiOBr-10h, and Bi–BiOBr are reported in Table S1, and show that crystallite sizes range between 15 and 18 nm. The length of the solvothermal process length didn't appear to alter the average crystal size of particles significantly. However, the size of BiOBr-CP (11.0 nm) is slightly smaller than those formed by the solvothermal method, which was attributed to this being a room-temperature synthesis.

The series of Bi/BiOBr/P25 composites, with Ti/Bi ranging from 0.2 to 6.6 were also examined by XRD, with their XRD patterns shown in Fig. 3. The XRD patterns of the P25 and Bi–BiOBr parent materials are also placed in Fig. 3 for reference. The results show that Bi–BiOBr–P 0.2, Bi–BiOBr–P 2.2, Bi–BiOBr–P 4.4, and Bi–BiOBr–P 6.6 adopt the expected tetragonal structure of BiOBr (BiOBr-ICSD-61225), along with peaks corresponding to the anatase (anatase-ICSD-142922) and rutile (rutile-ICSD-167954) phases of TiO_2 from P25. Additionally, the Bi metal (012) crystal plane can be observed in all patterns (Bi-ICSD-64703). The anatase (101) crystal plane overlaps with the BiOBr (011) crystal plane. Also, the rutile (110) crystal plane is very close to the Bi (012) crystal plane. The peak at ~25.3° belongs to the anatase (101) crystal plane, and the peak at ~27.5° corresponds to both the Bi (012) and rutile (110) crystal planes. By increasing the ratio of Ti/Bi in the Bi–BiOBr–P composites, the BiOBr (001) crystal plane increases in intensity, indicating that the presence of P25 particles during the solvothermal reaction promotes growth in this plane. Additionally, unlike the BiOBr series of samples, in Bi–BiOBr–P, the most prevalent peak was the (102) reflection followed by the (110) reflection, with a near analogous (102)/(110) peak ratio seen in all composite samples, indicating that the BiOBr particles in these samples are dominated by the (010) crystal plane (Mi et al., 2018).

In Fig. 3 the XRD pattern of the BiOBr–P 4.4-CP sample is also illustrated. The XRD pattern shows that BiOBr particles in BiOBr–P 4.4-CP are dominated by growth in the (001) crystal plane (Mi et al., 2018). This differed from the composites made by the solvothermal route, indicating the preferred orientation of crystal growth differs in samples made by the co-precipitation method. Xuelian et al., studied the effect of (001) and (010) crystal planes on the photocatalytic activity of BiOBr and saw that BiOBr containing predominantly (010) crystal planes exhibited enhanced photo-oxidative activity compared to BiOBr containing predominantly (001) crystal plane (Wu et al., 2017). Therefore, the Bi–BiOBr in the Bi–BiOBr–P composite is expected to have superior photo-oxidation performance compared to pure Bi–BiOBr with predominant growth in the (001) crystal planes.

The XRD patterns of Bi–BiOBr–P4.4–6h, Bi–BiOBr–P4.4 (12h), and Bi–BiOBr–P4.4–18h are shown in Fig. S7, revealing that the solvothermal synthesis duration increases the crystallinity of the samples and promotes the growth of (001) crystal plane of BiOBr in the composite.

3.6. Attenuated total reflectance-Fourier transform infrared (ATR-FTIR)

ATR-FTIR was used to study the IR active vibrational species in the

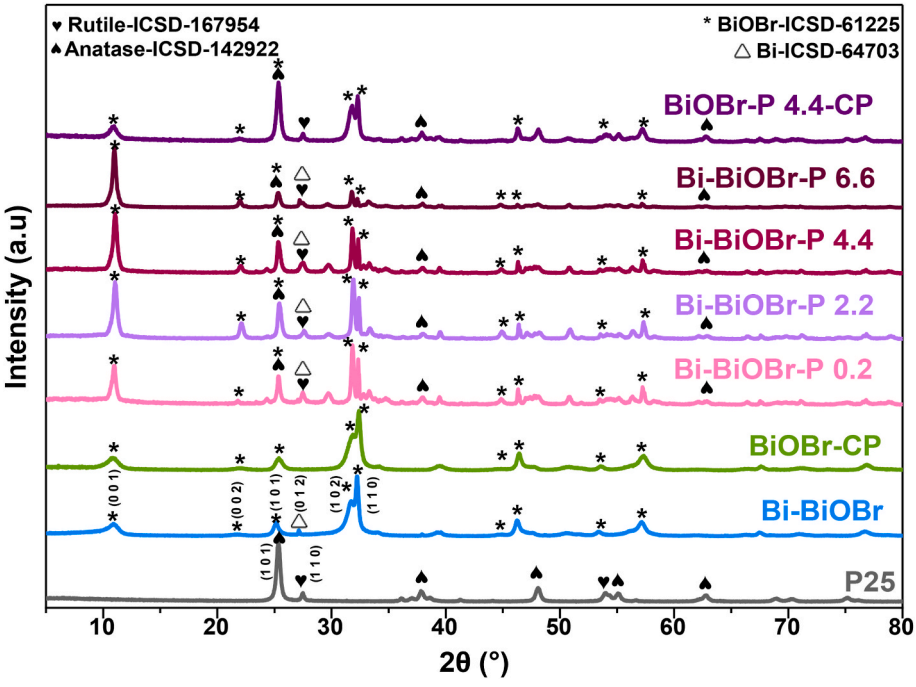

Fig. 3. XRD pattern of P25, Bi–BiOBr, Bi–BiOBr–P 0.2, Bi–BiOBr–P 2.2, Bi–BiOBr–P 4.4, and Bi–BiOBr–P 6.6 compared to Bi-ICSD-64703, BiOBr-ICSD-61225-4, anatase-ICSD-142922, rutile-ICSD-167954 standards.

structure of Bi–BiOBr (12h), P25, BiOBr-P-CP, and Bi–BiOBr–P 4.4, and the transmittance can be seen in Fig. S8. The Bi–BiOBr sample has a peak at 505 cm^{-1}, relating to the A_{2u}-type symmetrical vibrations of the Bi–O bond (Wang et al., 2011). The FT-IR spectrum of P25 shows a significant peak at 1645 cm^{-1} attributed to the bending vibration of Ti–OH, revealing the presence of hydroxyl functional groups on the surface of TiO_2. The peaks around 400 to 700 cm^{-1}, represent Ti–O stretching modes and Ti–O–Ti bridging stretching modes (Wang et al., 2012; Haque et al., 2017; Lopez et al., 1992). BiOBr-P-CP composite shows a series of peaks starting from 400 to 700 cm^{-1} assigned to Bi–O and Ti–O at 480 cm^{-1} Ti–O bending modes, with the 500 cm^{-1} stretch belonging to Bi–O bond vibrations, and Ti–O–Ti bridging stretching mode at 585 cm^{-1} (Wang et al., 2012; Zheng et al., 2020). Also, Bi–BiOBr–P 4.4 composite shows some peaks from 400 to 700 cm^{-1} but the peaks are not very clear. A significant peak at 1621 cm^{-1} can be assigned to the deformative vibration of Ti–OH stretching mode, and can be observed for Bi–BiOBr–P 4.4 and BiOBr-P-CP composites (Wang et al., 2011).

3.7. Raman spectroscopy

Fig. 4 presents the Raman spectra of P25, Bi–BiOBr, Bi–BiOBr–P 4.4, and BiOBr-P-CP from 50 to 1000 cm^{-1}. The Raman spectrum of P25 displays prominent peaks at 147 cm^{-1}, 399 cm^{-1}, 515 cm^{-1}, and 635 cm^{-1}, which can be attributed to the E_g, B_{1g}, $A_{1g} + B_{1g}$, and E_g modes of the anatase phase, respectively (Choi et al., 2005; Villabona-Leal et al., 2020). The spectrum of Bi–BiOBr shows peaks at 67 cm^{-1}, 110 cm^{-1} (corresponding to the A_{1g} internal Bi–Br stretching mode) and 142 cm^{-1} (corresponding to the E_{1g} internal Bi–Br stretching mode) and 370 cm^{-1} (corresponding to the B_{1g} phonon modes of oxygen atoms) (Davies, 1973; Zhang et al., 2013; Wang et al., 2014). The Raman spectrum of Bi–BiOBr–P 4.4 and BiOBr-P-CP depicts some peaks at 112 cm^{-1}, 150 cm^{-1}, 395 cm^{-1}, 514 cm^{-1}, and 633 cm^{-1} assigned to A_1g of BiOBr (internal Bi–Br stretching mode), and E_g, B_{1g}, $A_{1g} + B_{1g}$, and E_g modes of the anatase phase. Both Bi–BiOBr–P 4.4 and BiOBr-P-CP exhibit a redshift of the BiOBr bands compared to the parent materials. This red shift can be due to slight structural changes and variations in the lattice symmetry compared to the parent material (Wang et al., 2016).

3.8. Thermogravimetric analysis (TGA)

Fig. S9 illustrates the decomposition profiles of P25, Bi–BiOBr, and Bi–BiOBr–P 4.4, as analysed in air through thermogravimetric analysis. The mass losses for P25, Bi–BiOBr, and Bi–BiOBr–P 4.4 between 30 °C and 230 °C are 1.7%, 0.52%, and 0.5%, respectively. These losses are attributed to the evaporation of surface-adsorbed solvents from the synthesis process (e.g., water or ethylene glycol), as well as ambient-absorbed water. Bi–BiOBr is thermally stable below 230 °C; however, a 3.3% mass loss is observed between 230 °C and 450 °C due to the combustion of organic compounds. A further 17% mass loss occurs between 450 °C and 650 °C, corresponding to the formation of BiO and Br_2. The final 11% mass loss is seen from 650 °C to 900 °C, attributed to the decomposition of BiO and the formation of Bi_2O_3 (Mera et al., 2017; Chong et al., 2010; Song et al., 2010). Bi–BiOBr undergoes three distinct mass loss steps: 1.2% from 230 °C to 450 °C due to organic combustion, 2.3% from 450 °C to 550 °C due to the formation of BiO and Br_2, and 2.3% from 550 °C to 650 °C due to the formation of Bi_2O_3. It can be concluded that the Bi–BiOBr–P 4.4 composite exhibits enhanced thermal stability above 650 °C compared to Bi–BiOBr. This improved stability is likely due to the presence of P25 in the Bi–BiOBr–P 4.4 structure. P25 remains stable throughout the entire temperature range, with an overall mass loss of less than 3 wt%.

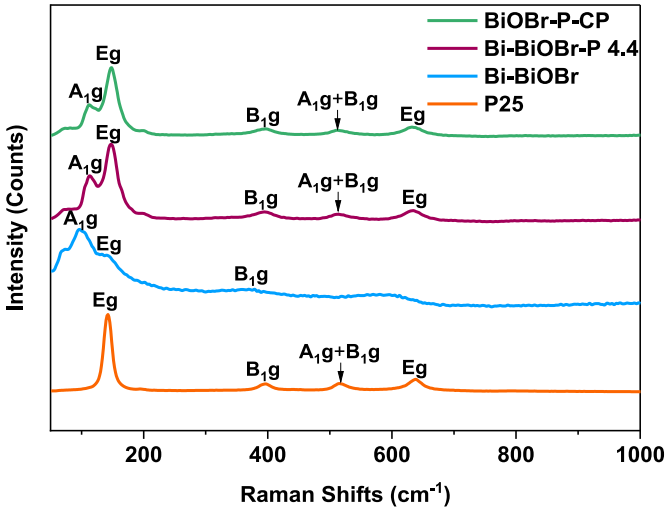

Fig. 4. Raman spectra of P25, Bi–BiOBr, Bi–BiOBr–P 4.4, and BiOBr-P-CP samples measured using a 532 nm laser from 50 to 1000 cm^{-1}.

3.9. UV–visible diffuse reflectance spectroscopy (DRS)

UV–visible diffuse reflectance spectroscopy (DRS) measurements were conducted in the wavelength range of 200–800 nm (Fig. 5). The diffuse reflectance data was transformed into the Kubelka-Munk function (F(R)), which is a unit proportional to absorbance according to the Kubelka-Munk relation (Equation (12)).

$$F(R) = \frac{K}{S} = \frac{(1-R)^2}{2R} \quad \text{Equation 12}$$

where R is the diffuse reflectance, and K and S denote the absorption and scattering coefficients, respectively. By employing the Tauc plot method (Equation (13)), we derived the indirect bandgap energy values. F(R) serves as a proxy for the absorption coefficient, denoted by α.

$$(F(R).hv)^{\frac{1}{2}} \quad \text{Equation 13}$$

where h represents Planck's constant and *v* signifies the frequency of light. These variables were plotted against energy, and by extrapolating to the energy axis, the bandgap was determined.

As shown in Fig. 5a, with an increase in reaction time for the series of BiOBr samples, an increase in enhanced visible light absorption is seen (with the exception of the 10h sample, which is an outlier to this trend). The increase in visible light absorption is attributed to an increased formation of Bi metal, as confirmed by XRD results, which can show broad plasmonic absorption across the visible light (Li et al., 2017). According to the calculation reported by Fang et al., the first absorption band of 10 nm-sized Bi nanoparticles should appear at around 270−280 nm (Fang et al., 2001/06; Wang et al., 2005), which can be seen in all Bi–BiOBr and BiOBr samples. The BiOBr-CP sample does not exhibit broad visible absorption, revealing the absence of Bi metal in its structure, and was in agreement with XRD results.

Based on Fig. 5a, the highest absorption in the visible region is seen in the Bi–BiOBr sample, which was solvothermally treated for the longest period of time. This indicates that a prolonged solvothermal treatment results in increased Bi metal formation, and therefore, increased plasmonic absorption in the visible region. As shown in Fig. 5b increasing the P25 loading mass in the series of Bi–BiOBr–P samples has made their optical behaviour more closely resemble that of P25. In Fig. 5c, the light absorption of Bi–BiOBr–P-4.4 and BiOBr–P 4.4-CP was compared.

Based on the literature, the absorption thresholds of pristine BiOBr and P25 are ~440 nm and ~410 nm, respectively (Yu et al., 2019; Zhang et al., 2008; Zhou et al., 2007), which are in broad agreement with the absorption spectra of the synthesised samples herein. Fig. 5 (d), (e) and (f) depict Tauc plots, showing the indirect allowed band gap transitions (Wang et al., 2012, 2013; Makuła et al., 2018). Although the Tauc plot of

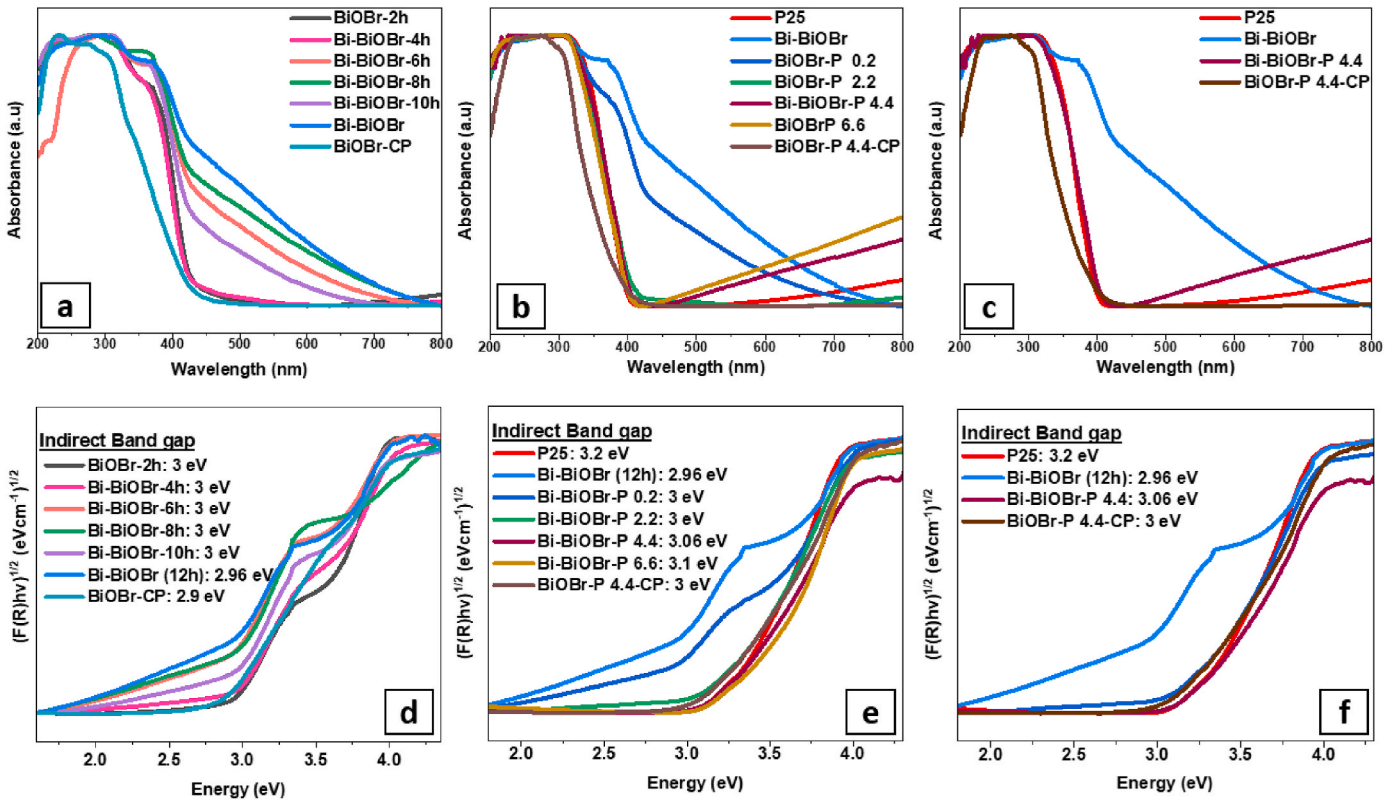

Fig. 5. Optical properties of Bi–BiOBr samples for a range of synthesis times and methods and Bi–BiOBr–P composite samples for a range of Ti/Bi atomic ratios. UV–visible absorption spectra of (a) Bi–BiOBr samples,(b) Bi–BiOBr–P samples, and (c) Bi–BiOBr–P 4.4 and BiOBr–P 4.4-CP samplesobtained by converting the measured values of diffuse reflectance to relative absorbance using the Kubelka-Munk relation. Tauc plots of (d) Bi–BiOBr samples, (e) Bi–BiOBr–P composite samples, and (f) Bi–BiOBr–P 4.4 and BiOBr–P 4.4-CP samples with the bandgap energy stated next to each sample name.

the Bi–BiOBr–P composites does not exhibit a specific difference in band gaps within this series of composites, the band gap of the composites is slightly wider than the band gap of the Bi–BiOBr (12h), as expected for composites diluted with a wider bandgap material.

3.10. X-ray photoelectron spectroscopy (XPS)

XPS measurements were conducted on Bi–BiOBr (12 h), P25, and Bi–BiOBr–P 4.4 composite to analyse their chemical composition and oxidation states, with Table 4 showing the atomic percentage of each element and Table S2 providing a summary of the binding energies of the key environments.

In Fig. S10, XPS scans of Bi–BiOBr (12h) display Br, Bi, O, and C. The Br 3d measurement shows two peaks corresponding to Br^- $3d_{7/2}$ (68.2 eV) and Br^- $3d_{5/2}$(69.2 eV) environments. The O 1s scan depicts two peaks, indicating the presence of Bi–O bonds (530.05 eV), and surface hydroxyl groups and/or organic C–O bonds (531.53 eV). The presence of C–O is likely from adventitious surface carbon species. The C 1s scan illustrates peaks corresponding to C–C (284.8 eV), C–O (286.37 eV), and C═O (288.46 eV) bonds that were attributed to adventitious carbon impurities adsorbed to the Bi–BiOBr surface. The Bi 4f scan shows four peaks indicating the presence of Bi^{3+} $4f_{7/2}$ (159.16 eV), Bi^{3+} $4f_{5/2}$ (164.48 eV), Bi^0 $4f_{7/2}$ (157.17 eV) and Bi^0 $4f_{5/2}$ (162.59 eV) (Yu et al., 2017). The main oxidation state of Bi is +3, however, metallic Bi^0 states are also observed, as a result of employing an ethylene glycol solvent that can act as a reducing agent in the solvothermal reaction at 180 °C, supported by our XRD and TEM results.

Table 4
The atomic percentage of the present elements in P25, Bi–BiOBr, and Bi–BiOBr–P 4.4 measured using XPS.

	Abundance (%)		
	Bi–BiOBr	**P25**	**Bi–BiOBr–P 4.4**
Bi^{3+}	88.05	–	4.51
Bi^0	0.46	–	0.96
O	5.44	52.57	62.24
Br	6.06	–	1.19
Ti	–	47.43	31.09

Fig. S11 shows the XPS scans of P25, showing C 1s, O 1s, and Ti 2p environments. The O 1s region of P25 depicts two peaks indicating the presence of Ti–O bond (530.17 eV), and surface adsorbed oxygen groups or organic C–O (531.18 eV). The C 1s scan shows peaks at 284.8 eV, 286.1 eV, and 289.23 eV, corresponding to C–C, C–O, and C═O bonds, respectively, that were assigned to adventitious carbon adsorbed to the P25 surface. In the Ti 2p region, Ti^{4+} $2p_{3/2}$ (458.93 eV) and Ti^{4+} $2p_{1/2}$ (464.77 eV) environments were observed, with no additional environments present. Previous literature has shown that these represent the expected binding energies for TiO_2 (Erdem et al., 2001). Fig. S12 shows the XPS scans of the Bi–BiOBr–P 4.4 composite, with Br 3d, Bi 4f, O 1s, C 1s, and Ti 2p environments. The Br 3d scan shows two peaks corresponding to Br^- $3d_{7/2}$ (68.13 eV) and Br^- $3d_{5/2}$ (69.13 eV). The Bi 4f scan contains 4 peaks at 159.07, 164.39, 156.98, and 162.3 eV corresponding to Bi^{3+} $4f_{7/2}$, Bi^{3+} $4f_{5/2}$, Bi^0 $4f_{7/2}$, and Bi^0 $4f_{5/2}$, respectively, similar to the B–BiOBr parent material. The C 1s scan shows peak binding energies of 284.8, 286.19, and 288.48 corresponding to C–C, C–O, and C═O, respectively (Al-Gaashani et al., 2019; Moeini et al., 2022). The C–O and C═O peaks are slightly shifted compared to P25, likely due to the presence of ethylene glycol residues in the composite. The O 1s of Bi–BiOBr–P 4.4 scan depicts 3 peaks indicating the presence of a metal–O bond (529.78 eV), O–C bond (530.98 eV), and surface O═C bond (531.97 eV). The metal–O bond shows a shift of ~0.5 eV in Bi–BiOBr–P 4.4 compared to the P25 and Bi–BiOBr parent samples,

indicating the O^{2-} sites in the metal–O bonds are likely more electron rich and therefore less strongly bound (Watts and Wolstenholme, 2019). In the Ti 2p scan of BiBiOBr–P 4.4, peaks corresponding to Ti^{4+} $2p_{3/2}$ (458.53 eV) and Ti^{4+} Ti $2p_{1/2}$ (464.24 eV) were observed.

In Fig. S13 we compare the Bi 4f, Ti 2p, C 1s, O 1s, and Br 3d scans of the Bi–BiOBr–P4.4 composite with Bi–BiOBr and P25. The Ti 2p scan of the composite showed a blue shift to higher binding energies compared to P25, indicating a reducing in electron density at Ti^{4+} sites, similar to results by Xn et al. (Tan et al., 2016). Based on the O and Ti core-level data, these shifts may be due to the formation of Ti–O–Bi bonds in the Bi–BiOBr–P 4.4 composite, due to chemical bonding interactions at the heterojunction between the BiOBr and TiO_2 phases (Tan et al., 2016). Based on the atomic abundances in Table 4, Bi–BiOBr exhibits a higher concentration of Bi^{3+} ions than anticipated, along with significantly lower atomic percentages of O and Br. This elevated Bi content may stem from the presence of oxygen vacancies, as confirmed by EDS analysis. Also, P25 shows a higher Ti^{4+} concentration than anticipated, likely resulting from oxygen vacancy formation during XPS analysis due to high vacuum and X-ray exposure. The Bi–BiOBr–P 4.4 composite shows a significantly lower Br level than expected which we postulate may be due to the less of Br upon forming Bi–O–Ti bonds. The empirical formula of the composite, based on the XPS quantitative analysis, is $Bi_{4.59}O_{52.3}BrTi_{26.12}$.

Low binding energy XPS analysis was conducted to determine the valence band maximum (E_{VBM}) energy levels of Bi–BiOBr, P25, and Bi–BiOBr–P 4.4 with respect to the Fermi level (E_F) of each material (Fig. S14), which were determined to be 2.16 eV, 2.43 eV, and 2.13 eV, respectively. The E_{VBM} could be adjusted to the NHE scale using E_F vs NHE from previous studies. The E_F potential of BiOBr with dominant (010) planes, similar to the composites formed by solvothermal synthesis in this work, was reported to be 0.6 V vs NHE (pH = 0) by Wu et al. (Wu et al., 2017; Li et al., 2024). And the E_F of P25 was reported to be −0.11 V vs NHE (pH = 0) (Cai et al., 2018; Li et al., 2021). Using the band gap values (E_g) obtained from Tauc plots, the conduction band minimum (E_{CBM}) energy was also obtained using Equation (9), as shown in Table 5. The low binding energy XPS results of Bi–BiOBr–P 4.4 was reported with respect to the E_F of the composite. Based on the measured E_{VBM}, E_{CBM}, and E_g, Bi–BiOBr is a n-type semiconductor, like P25.

$$E_{CBM} = E_{VBM} - E_g \quad \text{Equation 14}$$

3.11. N_2 sorption isotherms

N_2 sorption isotherms were measured at 77 K to determine the surface area and porosity of our samples (Fig. S15). In general, all samples show similar isotherm types, and therefore similar types of porosity. Specifically, all samples show Type II/III isotherms, typical of nonporous materials, with minor Type H3/H4 hysteresis loops, associated with narrow slit-shaped pores. As shown in Table 6, the P25 sample is the most porous, with a BET surface area of 54 m^2/g, and a total pore volume of 0.166 cm^3/g, likely due to its distinct nanoparticulate size-distribution. The least porous sample is Bi–BiOBr with a BET surface are of 18 m^2/g and a total pore volume of 0.043 cm^3/g. The Bi–BiOBr–P 4.4 composite has an intermediate surface area (37 m^2/g) and total pore volume (0.149 cm^3/g) between that of P25 and Bi–BiOBr. Therefore, we suggest that incorporating P25 to Bi–BiOBr helps enhance the porosity by embedding the P25 particles among Bi–BiOBr flakes. This is in accordance with our SEM analyses, which indicate the porosity of the Bi–BiOBr–P 4.4 appeares increased compared to Bi–BiOBr.

Table 5
Band potentials of Bi–BiOBr, P25 and Bi– BiOBr–P 4.4, including the band gaps (E_g), valence band maximum (E_{VBM}), conduction band minimum (E_{CBM}) and Fermi level (E_F) potentials vs NHE (at pH = X).

	Sample		
	Bi–BiOBr	P25	Bi–BiOBr–P4.4
E_g (V)	2.96 vs E_F (NHE)	3.20 vs E_F (NHE)	3.06 vs E_F
E_{VBM} (V)	2.76 vs E_F (NHE)	2.32 vs E_F (NHE)	2.13 vs E_F
E_{CBM} (V)	−0.2 vs E_F (NHE)	−0.89 vs E_F (NHE)	−0.93 vs E_F
E_F (V)	+0.60 (NHE) (Wu et al., 2017; Li et al., 2024)	−0.11 (NHE) (Li et al., 2021)	–

Table 6
Textural properties of Bi–BiOBr, P25, and Bi–BiOBr–P 4.4, as derived from N_2 sorption isotherms (77 K), including BET surface area (S_{BET}), total pore volume (V_{tot}), micropore volume (V_{micro}) and ratio of micropore volume to total pore volume ($V_{micro/tot}$).

Sample	S_{BET} (m^2/g)	V_{tot} (cm^3/g)	V_{micro} (cm^3/g)	$V_{micro/tot}$ (%)
Bi–BiOBr	18	0.043	0.018	42
P25	54	0.166	0.041	25
Bi–BiOBr–P 4.4	37	0.149	0.027	18

3.12. TAS

Transient absorption spectroscopy was conducted under atmospheric conditions on P25, Bi–BiOBr, and Bi–BiOBr–P 4.4 samples. These samples were excited using a 355 nm laser, and their dynamics of charge carriers were examined within the wavelength range of 600–1100 nm from 10 μs to 1 s (Fig. S16 and Fig. S17).

The decays were characterized by a power law function:

$$f(t) = At^{-\alpha} \quad \text{(Equation 15)}$$

where f(t) represents the concentration of charge carriers at time t, and A and α are fitting constants. This form of power law emerges when ideal bimolecular recombination (observed when $\alpha = 1$) is disrupted by a multiple-trapping process. In this process, a carrier must undergo repeated thermal excitations to the band-edge to facilitate movement and, eventually, recombination (Yu et al., 2023; Wang et al., 2018).

The model was used to analyse the transient absorption decays observed at the 800 nm probe wavelength, yielding α values of 0.114 (r^2 = 0.952), 0.185 (r^2 = 0.997), and 0.217 (r^2 = 0.978) for P25, Bi– BiOBr (12h), and Bi–BiOBr–P 4.4, respectively. The α values showed that the charge carrier motion and trapping behaviour of Bi–BiOBr–P 4.4 were more similar to Bi–BiOBr compared to P25. Additionally, the α value of Bi–BiOBr–P 4.4 was more similar to Bi–BiOBr than that of P25. This was supported by the similar lifetime of charge carriers seen in Fig. 6 for Bi–BiOBr and Bi–BiOBr–P 4.4, shown by $t_{50\%}$ (*i.e.* the time taken for the transient absorption to decay to 50% of its original value seen at 10 μs after the laser pulse) of ~160 μs and 200 μs, and complete decay by ~1 s after the laser pulse, respectively. The photogenerated charge carriers are significantly longer lived in P25, with a $t_{50\%}$ of 3800 μs seen. Nevertheless, a higher initial degree of transient absorption was seen in Bi–BiOBr–P 4.4 composite compared with P25, which was indicative of a higher initial charge carrier population. This indicates that on the pre-μs timescale, charge carrier separation was improved in the Bi–BiOBr–P 4.4 composite as compared with P25. Based on these studies using 355 nm excitation, our results indicate that charge transfer occurs from P25 to BiOBr, most likely due to electron transfer from the CBM of P25 to the CBM of BiOBr (Fig. 9). This is because the composite behaves more similarly to the Bi–BiOBr parent material, despite the majority of the material being composed of P25 (Ti/Bi ratio = 4.4).

For the Bi–BiOBr sample at 10 μs, 100 μs, 1 ms, and 10 ms, a broad transient absorption was seen across the visible, with stronger absorption in the green and weaker absorption in the near-infrared (NIR) (Fig. S17). However, for P25 and Bi–BiOBr–P 4.4, a maximum absorption was seen at ~700 and 800 nm, with weaker absorption seen in the green and NIR at 10 μs compared to Bi–BiOBr. Previous transient

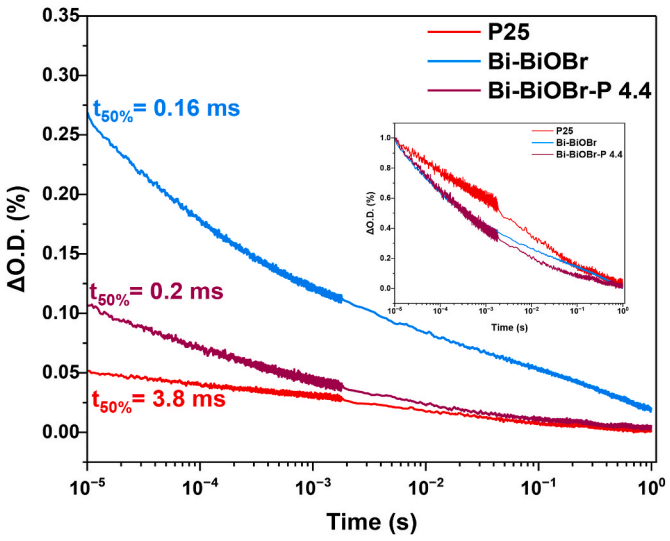

Fig. 6. Transient absorption decay kinetics for Bi–BiOBr (12h), P25, and Bi–BiOBr–P 4.4 samples measured from 10 μs to 1 s after excitation with a laser (355 nm, 6ns width, ~220 μJ cm^{-2} per pulse) and measured at a probe wavelength of 800 nm.

absorption studies of BiOBr have been conducted on the ultrafast timescale (i.e., fs – ns), revealing that oxygen vacancy in BiOBr crystalline structure can trap electrons during the relaxation process after excitation (Wang et al., 2018). A slower timescale study on a BiOI semiconductor shows a similar transient absorption spectrum to BiOBr with a significantly faster decay rate ($t_{50\%}$–45 μs) (Quan et al., 2023).

3.13. Photocatalytic activity

The photocatalytic activity of all samples produced herein, listed in Table 2, was evaluated against NO gas in accordance with ISO, 22197–1:2016, standard protocol. The best-performing sample, which was a composite composed of Bi/BiOBr/P25 (sample Bi–BiOBr–P 4.4) was also evaluated against NO_2 gas along its parent materials.

Bi–BiOBr samples produced by a 12 h solvothermal treatment showed the highest photocatalytic activity towards NO gas (Fig. S18), and was therefore taken forward for making a series of composites with P25 (with the atomic ration of Ti/Bi ranging from 0.2 to 6.6). A BiOBr counterpart made using a co-precipitation method was also evaluated for comparison with samples made by our solvothermal method.

The results for experiments conducted under visible light are summarised in Fig. 7a. Although the photocatalytic activity of the sample made by the co-precipitation method (BiOBr-CP) showed higher NO reduction (11.2%) and NO_x removal (5.6%) than its counterpart made by the solvothermal method (Bi–BiOBr), it generated significantly more NO_2 (5.5%). Under visible light, P25 showed higher photocatalytic activity than both BiOBr-CP and Bi–BiOBr samples, which was attributed to the light source containing some emission in the UVA. Upon forming a composite between Bi–BiOBr and P25, the activity was seen to increase with the Ti/Bi atomic ratio, where an optimum value was seen at 4.4 in sample Bi–BiOBr–P 4.4. This sample showed an NO removal of 32.8%, which was higher than the sum of its parent materials Bi–BiOBr (6.7%) and P25 (21.2%), indicating a synergetic interaction between these two materials in the composite. This favourable interaction was not seen in the composite made using BiOBr from our co-precipitation method, where a lower NO removal of 12.8% was seen compared with P25 alone (21.2%).

The results for UVA light are summarised in Fig. 7b. The activity of samples, in general, is significantly higher under UVA irradiation compared to visible light irradiation. The best performing composite under visible light, Bi–BiOBr–P 4.4 (55.3%), shows similar NO removal

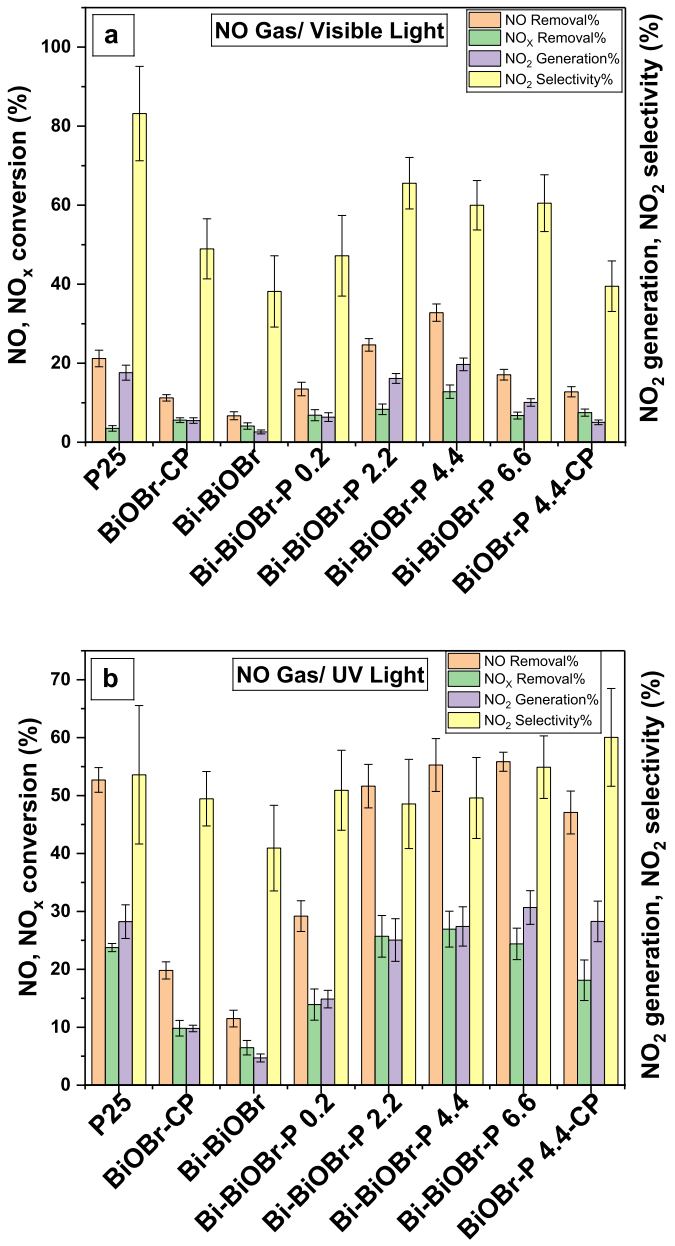

Fig. 7. Photocatalytic NO removal tests for the series of Bi/BiOBr/P25 composites produced herein and their parent materials summarising their NO removal (%), NO_x removal (%), NO_2 generation (%) and NO_2 selectivity (%), examined under (a) visible light (300–800 nm), and (b) UVA light.

activity to P25 (52.7%). Therefore, no synergetic enhancement is seen under UVA irradiation.

Nevertheless, the best-performing composite, which matches the activity of P25 under UVA light and surpasses the activity of P25 under visible light, is Bi–BiOBr–P 4.4. The photocatalytic activity of this composite and its parent materials were tested against NO_2 gas under visible and UVA light (Fig. 8). The Bi–BiOBr–P 4.4 composite showes higher than the summative performance of its parent materials under both light conditions, displaying a NO_x removal of 15.1% and 29.5% under visible and UV light, respectively. This indicates that a synergetic enhancement happens in reactions with NO_2 gas under both visible and UV light conditions for the Bi–BiOBr–P 4.4 composite with respect to its parent materials. Unlike its parent materials, the Bi–BiOBr–P 4.4 composite does not generate any NO gas during the conversion of NO_2, indicating that the NO_2 gas is completely converted to nitrate. The surface copmosition of the Bi–BiOBr–P 4.4 composite after the NO and

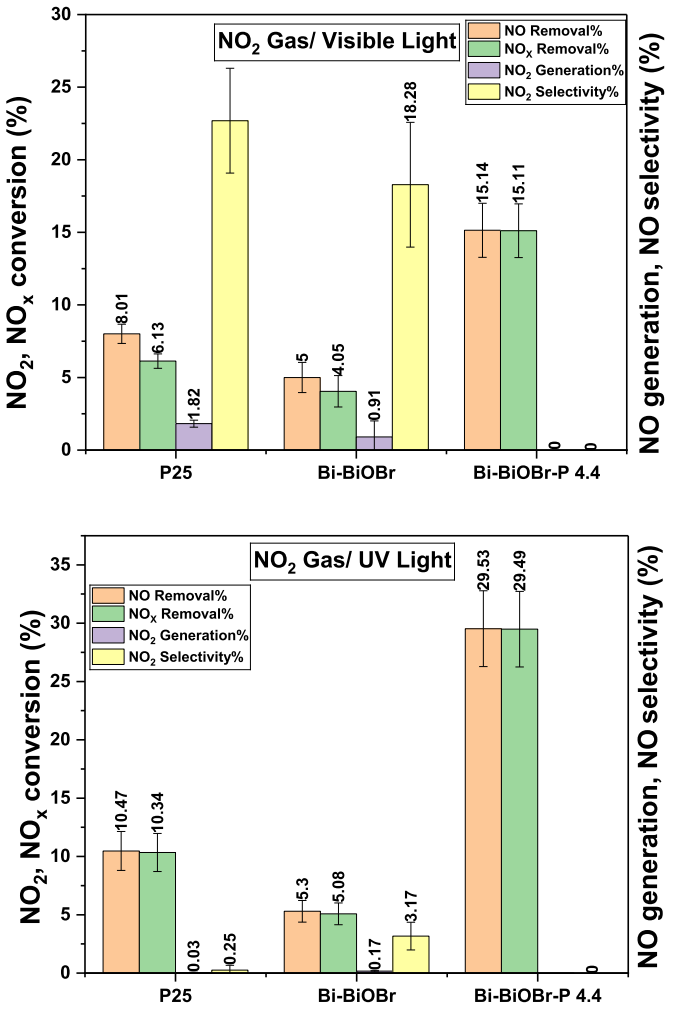

Fig. 8. NO_2 removal tests of P25, Bi–BiOBr (12h), and Bi–BiOBr–P 4.4 under (a) visible light (Daylight lamp with a range of 300–800 nm wavelength), and (b) UV light.

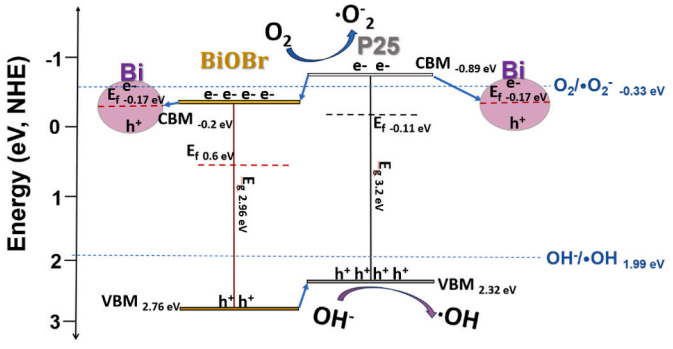

Fig. 9. Band energy diagram of the Bi/BiOBr/P25 composite – sample Bi–BiOBr–P 4.4 – plot alongside the oxidation and reduction potentials of forming reactive oxygen species (ROS) that can drive the oxidation of NO_x.

NO_2 tests was investigated by ATR-FTIR (Fig. S19). After tests with NO gas, peaks at 1290 cm^{-1} and 1420 cm^{-1} appeared, revealing that monodentate nitrate was present on the surface, as well as a small peak for bidentate nitrate formation at 1621 cm^{-1} (Mihaylov et al., 2021). Additionally, after tests with NO_2 gas, similar peaks where observed to the tests with NO, but with a reduced level of monodentate nitrate and increased level of bidentate nitrate seen (Mihaylov et al., 2021).

To study the versatility of the best performing Bi–BiOBr–P 4.4 composite, the photocatalytic activity towards NO gas was examined at a range of additional conditions, as shown in Fig. S20. Four variables were considered: relative humidity percentage (RH%: 7%, 50%, or 100%), UV light intensity (1 mW cm^{-2} or 2.36 mW cm^{-2}, 1 ppm NO concentration with a 3 L min^{-1} flowrate or 3 ppm NO concentration with a 1 L min^{-1} flowrate). The highest NO removal (87.2%) performance was achieved under 7% relative humidity, 2.36 mW cm^{-2} UV light intensity, 3 ppm NO initial concentration, and a 1 L min^{-1} flow rate. A similar relative humidity and light level can be found in extremely dry and hot cities like Yazd (Iran), Las Vegas (USA), and Riyadh (Saudi Arabia) condition Under ISO conditions, the performance over five cycles of testing was also studied, as illustrated in Fig. S21. After each consecutive run, the NO_2 generation incrementally increased and NO removal incrementally decreased. This showed the active sites of the composite were blocked with the successive buildup of nitric acid on its surface, which can drive a back reaction and formation of NO and NO_2 (Mills and Elouali, 2015). After five cycles, the sample was placed in a container filled with DI water for 30 min, followed by drying at 60 °C in an oven for 2h. The washed sample was tested again, and the activity was seen to be restored to near its original level.

The figure of merit (FOM) was also determined from the NO gas removal tests for P25, BiOBr-CP, Bi–BiOBr (12h), Bi–BiOBr–P 0.2, Bi–BiOBr–P 2.2, Bi–BiOBr–P 4.4 and Bi–BiOBr–P 6.6 samples (Fig. S22). The FOM was calculated using Equation (8), which considers the negative effect of NO_2 generation three times more than its ability to remove NO. Since the measured FOMs are negative, the highest FOM under UV light belongs to the Bi–BiOBr sample, and the highest FOM under visible light belongs to the BiOBr-CP sample. The FOM of Bi–BiOBr, P25, and Bi–BiOBr–P 4.4 was also determined for tests using NO_2 gas, shown in Fig. S23. Under both UV and visible light, the highest FOM belonged to Bi–BiOBr–P 4.4 (FOM $(NO_2)_{UV}$ ~1.3; FOM $(NO_2)_{visible}$ ~0.2), which was synergistically higher than its parent materials Bi–BiOBr and P25, especially for tests conducted using UV light.

The NO deposition velocity (V_d) was determined for the P25, BiOBr-CP, Bi–BiOBr (12h), Bi–BiOBr–P 0.2, Bi–BiOBr–P 2.2, Bi–BiOBr–P 4.4, Bi–BiOBr–P 6.6, and BiOBr–P 4.4-CP samples, using Equation (10), and shown in Fig. S24. The deposition velocity (V_d) is an important measure for comparing NO removal outcomes across different NOx gas concentrations, flow rates, or sample areas. It represents the rate at which NO accumulates on the surface of the photocatalyst (Sanchez et al., 2021), and can be used to predict photocatalytic efficiency under specific conditions (Engel et al., 2015). In this study, the Bi–BiOBr–P 4.4 composite, identified as the most active photocatalyst herein, exhibited a higher V_d than P25 and Bi–BiOBr, both under UV light (0.77 cm/s) and visible light (0.38 cm/s).

3.13.1. *The mechanism of photocatalytic action*

Based on the determined energy levels of Bi metal, BiOBr, and P25, shown in Fig. 9, there is a thermodynamic driving force for photogenerated electrons to move from the CB of P25 to the CB of BiOBr. There is also a driving force for electrons to move from the CB of both P25 and BiOBr to Bi sites. This indicates that electrons will accumulate in BiOBr and/or Bi sites. On the other hand, there is a driving force for photogenerated holes to move from the VB of BiOBr to the VB of P25, which indicates that holes will likely accumulate in P25. Overall, the band energy offset between BiOBr and P25 forms a type II staggered heterojunction that drives the vectoral separation of electrons and holes in opposing directions. This band energy diagram is in line with our TAS results that show how charge transfer between P25 to Bi–BiOBr sites occurred. Due to the wide gap in energy between the VBM and Fermi levels it was concluded that the BiOBr synthesised was n-type, the same as P25.

The suggested mechanism for the photocatalytic action of the Bi/BiOBr/P25 composite is shown in Fig. 9. The redox potential of O_2 reduction to $^{\bullet}O_2^-$ radicals is −0.33 V (vs NHE) (Sun et al., 2023), and as

the E_{CBM} of P25 is more negative, it is capable of producing $^{\bullet}O_2^-$ radicals. Alongside this, the oxidation potentials of ^-OH to $^{\bullet}OH$ and H_2O to $^{\bullet}OH$ are +1.99 V (vs NHE) and +2.30 V (vs NHE) (Sun et al., 2023), respectively, and both BiOBr and P25 have a more positive E_{VBM} and are capable of producing hydroxyl radicals. However, since the energy offset encourages the accumulation of holes in P25, we believe that P25 plays a major role in producing $^{\bullet}OH$ radicals. Also, as both the Bi-metal and BiOBr sites accumulate electrons, but do not possess a sufficiently negative E_{CBM} to drive $^{\bullet}O_2^-$ formation, we speculate that the oxidation of NO and NO_x is predominantly driven by $^{\bullet}OH$ radicals on our photocatalyst.

3.13.2. Comparisons with BiOBr and P25 in the literature

Many studies have investigated the photocatalytic activity of TiO_2 and BiOX (X = Cl, Br and I) towards NO_x pollution, as shown in Table 7.

In one study, BiOBr was synthesised by Montoya-Zamora et al. using the microwave-assisted co-precipitation method, showing a high photocatalytic activity of 94% NO removal with a selectivity to form nitrate ions of 98% (Montoya-Zamora et al., 2020). Additionally, Montoya-Zamora tested the photocatalytic activity of the benchmark photocatalyst P25 under the same conditions and reported approximately 4 times lower NO removal activity. $BiOBr/Bi_{24}O_{31}Br_{10}$ was synthesised by Cruz et al. using a simple co-precipitation method. The photocatalyst oxidised 90% of NO with nitrate selectivity at 93% (Martínez-de la Cruz et al., 2024). A $BiOBr/C_3N_4$ composite photocatalyst prepared by Yanjuan Sun et al. showed 32.7% NO removal (Sun et al., 2014). Li et al., synthesised a z-scheme $BiOBr/Bi_{12}O_{17}Br_2$ photocatalyst employing a hydrolysis method, which showed superior performance for NO removal (57.3%) compared to the parent materials (Li et al., 2019). Shi et al. used a solvothermal method to synthesise a BiOBr/BiOI heterojunction photocatalyst, which showed 57% NO removal (Shi et al., 2019). Mendoza et al. examined the NO removal photocatalytic activity of TiO_2 under UV light and reported 64% NO removal (Mendoza et al., 2016). The NO photo-oxidation performance was increased (>90% NO removal) by coating a zeolite with TiO_2. Zhao et al. fabricated a heterojunction of TiO_2/BiOCl using a solvothermal method and its NO photo-oxidation showed 75% NO removal (Zhao et al., 2023). Jiamprasertboon et al. synthesised nanostructured BiOCl films using aerosol-assisted chemical vapor deposition (AACVD) with various solvents. Among the samples, the BiOCl synthesised using ethyl acetate exhibited the highest NO removal efficiency of 1.18% under UV light (Jiamprasertboon et al., 2022). Quan et al. synthesised a Bi/BiOI composite using a solvothermal method and tested it for NO gas removal under UV and visible light. The composite achieved NO removal rates of 33.1% under UV light and 26.3% under visible light (Quan et al., 2023).

In this study, Bi–BiOBr–P 4.4 shows the superior performance compared to other samples and parent materials with an NO removal%, NO_x removal%, and NO_2 generation% of 32.8%, 12.8%, and 19.7% under visible light (300 nm–800 nm), respectively. This composite shows an NO removal%, NO_x removal%, and NO_2 generation% of 55.27%, 26.94%, and 27.4% under UV light, respectively. Under optimised conditions, the highest NO removal%, NO_x removal%, and NO_2 generation% using this composite were 87.2%, 55.03%, and 30.39%, respectively. The optimised condition, in terms of UV intensity (2.36 mW cm^{-2}) and relative humidity (7%) can be found in cities with intense sunlight and dry climates like Las Vegas, USA; Riyadh, Saudi Arabia; and Yazd, Iran.

Comparisons of the performances seen by other researchers and the materials studied herein are challenging. This is because in many previous studies unconventional reactor geometries, sample sizes, light sources and powers, pollutant concentrations, relative humidities, and gas flow rates have been examined, which do not conform to the prescribed ISO protocol (22197–1:2016) used herein. Nevertheless, herein, the deposition velocity (V_d), which accounts for some differences in test conditions, was determined for tests conducted using NO gas, where our best performing Bi–BiOBr–P 4.4 showed a V_d of 0.77 cm/s under UV light 0.38 cm/s under visible light. This was significantly higher performing than a commercial mineral silicate paint containing TiO_2 (0.05 cm/s) and a commercial acrylic paint containing TiO_2 (0.13 cm/s), both tested under UV light (Maggos et al., 2007). Additionally, Quan et al. measured the V_d of Bi/BiOI under UV light, revealing a lower performance of 0.42 cm/s compared to the Bi–BiOBr–P 4.4 composite (Quan et al., 2023).

4. Conclusion

In this research, a range of Bi/BiOBr/P25 TiO_2 composites and their parent materials were synthesised and examined for their ability to drive the photocatalytic conversion of NO_x gas pollution. Two different synthetic routes were examined, with the most active composite found to be produced using a solvothermal method for a 12 h reaction with a Ti/Bi ratio of 4.4 (herein named Bi–BiOBr–P 4.4). SEM, TEM and XRD showed that the most active composite was composed of Bi nanoparticles ~5 nm in diameter P25 nanoparticles ~15 nm in diameter that decorated

Table 7
NO_x removal photocatalytic activity of photocatalysts containing BiOX (X = Cl, Br, I) and TiO_2 from the literature compared with the performance of photocatalysts produced herein.

Material	Target pollutant	ISO	RH(%)	Pollutant removal%	Light source	Pollutants concentration	Ref.
BiOBr/60% EDTA	NO gas	Yes	50%	94%	3 LED lamp (24 W)	1 ppm	Montoya-Zamora et al. (2020)
P25	NO gas	Yes	50%	24%	3 LED lamp (24 W)	1 ppm	Montoya-Zamora et al. (2020)
$BiOBr/Bi_{24}O_{31}Br_{10}$	NO gas	Yes	50%	90%	40 W fluorescent lamp	1 ppm	Martínez-de la Cruz et al. (2024)
2D $BiOBr/C_3N_4$	NO gas	No	ns	32.7%	100 W tungsten halogen lamp (420 nm cut-off filter)	600 ppb	Sun et al. (2014)
$BiOBr/Bi_{12}O_{17}Br_2$	NO gas	ns	50%	57.3%	500W xenon lamp	400 ppm	Li et al. (2019)
BiOBr/BiOI	NO gas	No	ns	57%	Xenon lamp	600 ppb	Shi et al. (2019)
TiO_2-coated zeolite	NO gas	No	40–60%	>90%	6 × UV-A lamp 20 W	<5 ppm	Mendoza et al. (2016)
TiO_2/BiOCl (Ti:Bi/4:1)	NO gas	No	ns	75%	Xenon lamp 300 W	200 ppm	Zhao et al. (2023)
BiOCl	NO gas	Yes	50%	1.18%	2 × Sankyo (UV lamp), 15 W	2.5 ppm	Jiamprasertboon et al. (2022)
Bi/BiOI	NO gas	Yes	50%	33.1%	2 × Sankyo (UV lamp), 15 W	1 ppm	Quan et al. (2023)
Bi/BiOI	NO gas	Yes	50%	26.3%	2 × Sylvania (visible lamp), 15 W	1 ppm	Quan et al. (2023)
Bi–BiOBr–P 4.4	NO gas	Yes	50%	54.9%	2 × Sankyo (UV lamp), 15 W	1 ppm	This study
Bi–BiOBr–P 4.4	NO gas	Yes	7%	87.2%	2 × Sankyo (UV lamp), 15 W	1 ppm	This study

ns = not stated.

tetragonal structured BiOBr lamellar flakes; where these composite flakes formed a larger sponge-like superstructure ~3–5 μm in diameter. N_2 sorption isotherms of Bi–BiOBr–P 4.4 revealed a total pore volume of 0.149 cm^3/g, micropore volume of 0.027 cm^3/g and surface area of 37.1 m^2/g. XPS results identified chemical bonding interactions between BiOBr and P25, and alongside diffuse reflectance spectroscopy (DRS), was used to determine the band energy diagram, where a staggered type II heterojunction was formed. TAS results showed that charge transfer on the pre-μs timescale was occurring between BiOBr and P25 sites, increasing the population of charge carriers relative to P25 alone.

The photocatalytic activity of Bi–BiOBr–P 4.4, was examined against NO (32.8% under visible light; 55.3% under UVA light) and NO_2 (15.1% under visible light; 29.5% under UVA light) gas, showing synergetic increases in activity with respect to its parent materials P25 and Bi-BiOBr. A range of conditions were examined, where it was found that at low relative humidity (~7%), higher UVA light intensity (~2.36 mW cm^{-2}) and higher NO concentration (~3.0 ppm) and slower flow rate (~1.0 L min^{-1}) a higher NO removal rate of 87.2% was observed. It was therefore concluded that our optimal composite photocatalyst shows promise for applications in extremely dry climates with intense sunlight.

CRediT authorship contribution statement

Paransa Alimard: Writing – review & editing, Writing – original draft, Methodology, Investigation, Formal analysis, Data curation, Conceptualization. **Chen Gong:** Writing – review & editing, Methodology, Investigation, Formal analysis. **Ioanna Itskou:** Writing – review & editing, Methodology, Formal analysis. **Andreas Kafizas:** Writing – review & editing, Writing – original draft, Supervision, Resources, Formal analysis.

Declaration of Competing Interest

The authors declare that they have no known competing financial interests or personal relationships that could have appeared to influence the work reported in this paper.

Acknowledgments

The authors gratefully acknowledge Professor Camille Petit from Department of Chemical Engineering of Imperial College London, United Kingdom, for conducting N_2 sorption studies. P. A. thanks the Science and Solutions for a Changing Planet DTP (NE/S007415/1), hosted at the Grantham Institute for Climate Change and the Environment, Imperial College London, United Kingdom, for funding this research. A. K. thanks the EPSRC for a Programme Grant (EP/W017075/1) and the Royal Society for an Equipment Grant (RSG/R1/180434). I.I thanks the Chemical Engineering Department of Imperial College London for a Departmental PhD Scholarship.

Appendix A. Supplementary data

Supplementary data to this article can be found online at https://doi.org/10.1016/j.chemosphere.2024.143728.

Data availability

Data will be made available on request.

References

Al-Gaashani, R., Najjar, A., Zakaria, Y., Mansour, S., Atieh, M., 2019. XPS and structural studies of high quality graphene oxide and reduced graphene oxide prepared by different chemical oxidation methods. Ceram. Int. 45 (11), 14439–14448.
Ângelo, J., Andrade, L., Madeira, L.M., Mendes, A., 2013. An overview of photocatalysis phenomena applied to NOx abatement. J. Environ. Manag. 129, 522–539.
Ao, C., Lee, S., Mak, C.L., Chan, L., 2003. Photodegradation of volatile organic compounds (VOCs) and NO for indoor air purification using TiO2: promotion versus inhibition effect of NO. Appl. Catal. B Environ. 42 (2), 119–129.
Brunauer, S., Emmett, P.H., Teller, E., 1938. Adsorption of gases in multimolecular layers. J. Am. Chem. Soc. 60 (2), 309–319.
Cai, H., Cheng, L., Xu, F., Wang, H., Xu, W., Li, F., 2018. Fabrication of the heterojunction catalyst BiVO4/P25 and its visible-light photocatalytic activities. R. Soc. Open Sci. 5 (8), 180752.
Choi, H.C., Jung, Y.M., Kim, S.B., 2005. Size effects in the Raman spectra of TiO2 nanoparticles. Vib. Spectrosc. 37 (1), 33–38.
Chong, M.N., Jin, B., Chow, C.W., Saint, C., 2010. Recent developments in photocatalytic water treatment technology: a review. Water Res. 44 (10), 2997–3027.
Davies, J., 1973. Solid state vibrational spectroscopy—III [1] the infrared and Raman spectra of the bismuth (III) oxide halides. J. Inorg. Nucl. Chem. 35 (5), 1531–1534.
Dong, F., et al., 2014. A semimetal bismuth element as a direct plasmonic photocatalyst. Chem. Commun. 50 (72), 10386–10389.
Dubinin, M., 1947. The Equation of the Characteristic Curve of Activated Charcoal, vol. 55. Dokl. Akad. Nauk. SSSR, pp. 327–329.
Engel, A., Glyk, A., Hülsewig, A., Große, J., Dillert, R., Bahnemann, D.W., 2015. Determination of the photocatalytic deposition velocity. Chem. Eng. J. 261, 88–94.
Erdem, B., Hunsicker, R.A., Simmons, G.W., Sudol, E.D., Dimonie, V.L., El-Aasser, M.S., 2001. XPS and FTIR surface characterization of TiO2 particles used in polymer encapsulation. Langmuir 17 (9), 2664–2669.
Fang, J., et al., 2001. Microemulsion-processed bismuth nanoparticles. Mater. Sci. Eng., B 83 (1), 254–257. https://doi.org/10.1016/S0921-5107(01)00528-1.
Fthenakis, V., Lynn, P.A., 2010. Electricity from Sunlight Photovoltaic- Systems Integration and Sustainablility. WILEY.
Gondal, M.A., Xiaofeng, C., Dastageer, M.A., 2017. Novel Bismuth-Oxyhalide-Based Materials and Their Applications. Springer.
Hailili, R., Li, Z., Lu, X., Sheng, H., Bahnemann, D.W., Zhao, J., 2024. Ultrathin defective heterojunction for visible light NO removal: correlation between microstructure and reaction mechanisms. Environ. Sci. Nano. 11, 3301–3316.
Haque, F.Z., Nandanwar, R., Singh, P., 2017. Evaluating photodegradation properties of anatase and rutile TiO2 nanoparticles for organic compounds. Optik 128, 191–200.
Hermawan, A., Hasegawa, T., Asakura, Y., Yin, S., 2021. Enhanced visible-light-induced photocatalytic NOx degradation over (Ti, C)-BiOBr/Ti3C2Tx MXene nanocomposites: role of Ti and C doping. Separ. Purif. Technol. 270, 118815.
Horikoshi, S., et al., 2011. Molecular dynamics simulations of adsorption of hydrophobic 1, 2, 4-trichlorobenzene (TCB) on hydrophilic TiO2 in surfactant emulsions and experimental process efficiencies of photo-degradation and-dechlorination. J. Photochem. Photobiol. Chem. 217 (1), 141–146.
Huo, Y., Zhang, J., Miao, M., Jin, Y., 2012. Solvothermal synthesis of flower-like BiOBr microspheres with highly visible-light photocatalytic performances. Appl. Catal. B Environ. 111, 334–341.
Jiamprasertboon, A., et al., 2022. Photocatalytic NO x oxidation of BiOCl nanostructure-based films grown using aerosol-assisted chemical vapor deposition. ACS Appl. Nano Mater. 6 (1), 738–749.
Juntrapirom, S., et al., 2021. Natural sunlight driven photocatalytic coupling of primary amines over TiO2/BiOBr heterojunction. Appl. Surf. Sci. 545, 149015.
Kang, Y., Yang, Y., Yin, L.C., Kang, X., Liu, G., Cheng, H.M., 2015. An amorphous carbon nitride photocatalyst with greatly extended visible-light-responsive range for photocatalytic hydrogen generation. Adv. Mater. 27 (31), 4572–4577.
Kato, C., 2020. "Corrosion in Nuclear Fuel Reprocessing Plants: Corrosion in Boiling Nitric Acid,".
Ku, Y., Tseng, K.Y., Ma, C.M., 2008. Photocatalytic decomposition of gaseous acetone using TiO2 and Pt/TiO2 catalysts. Int. J. Chem. Kinet. 40 (4), 209–216.
Leary, R., Westwood, A., 2011. Carbonaceous nanomaterials for the enhancement of TiO2 photocatalysis. Carbon 49 (3), 741–772.
Li, X., Wang, D., Cheng, G., Luo, Q., An, J., Wang, Y., 2008. Preparation of polyaniline-modified TiO2 nanoparticles and their photocatalytic activity under visible light illumination. Appl. Catal. B Environ. 81 (3–4), 267–273.
Li, X., Yu, J., Jaroniec, M., 2016. Hierarchical photocatalysts. Chem. Soc. Rev. 45 (9), 2603–2636.
Li, X., et al., 2017. Activation of amorphous bismuth oxide via plasmonic Bi metal for efficient visible-light photocatalysis. J. Catal. 352, 102–112.
Li, R., Xie, F., Liu, J., Zhang, C., Zhang, X., Fan, C., 2019. Room-temperature hydrolysis fabrication of BiOBr/Bi12O17Br2 Z-Scheme photocatalyst with enhanced resorcinol degradation and NO removal activity. Chemosphere 235, 767–775.
Li, G., Huang, R., Zhu, C., Jia, G., Zhang, S., Zhong, Q., 2021. Effect of oxygen vacancies and its quantity on photocatalytic oxidation performance of titanium dioxide for NO removal. Colloids Surf. A Physicochem. Eng. Asp. 614, 126156.
Li, X., et al., 2022. Growth of BiOBr/ZIF-67 nanocomposites on carbon fiber cloth as filter-membrane-shaped photocatalyst for degrading pollutants in flowing wastewater. Advanced Fiber Materials 4 (6), 1620–1631.
Li, X., et al., 2023. Effect of oxygen vacancies on the photocatalytic activity of flower-like BiOBr microspheres towards NO oxidation and CO2 reduction. Separ. Purif. Technol. 309, 123054.
Li, X., et al., 2024. Defective Bi@ BiOBr/C microrods derived from Bi-MOF for efficient photocatalytic NO abatement: directional regulation of interfacial charge transfer via carbon–loading. Appl. Catal. B Environ. 340, 123238.
Lopez, T., Sanchez, E., Bosch, P., Meas, Y., Gomez, R., 1992. FTIR and UV-Vis (diffuse reflectance) spectroscopic characterization of TiO2 sol-gel. Mater. Chem. Phys. 32 (2), 141–152.
Ma, D., Zhao, J., Zhao, Y., Hao, X., Lu, Y., 2012. An easy synthesis of 1D bismuth nanostructures in acidic solution and their photocatalytic degradation of rhodamine B. Chem. Eng. J. 209, 273–279. https://doi.org/10.1016/j.cej.2012.08.021.

Maggos, T., Bartzis, J.G., Leva, P., Kotzias, D., 2007. Application of photocatalytic technology for NO x removal. Appl. Phys. A 89, 81–84.
Makuła, P., Pacia, M., Macyk, W., 2018. How to Correctly Determine the Band Gap Energy of Modified Semiconductor Photocatalysts Based on UV–Vis Spectra, vol. 9. ACS Publications, pp. 6814–6817.
Martínez-de la Cruz, A., Reyna-Cavazos, K., Cuéllar, E.L., Ibarra, R.M., 2024. "Photocatalytic Characterization of BiOCl and BiOBr Prepared by Polyol-Assisted Coprecipitation for the Elimination of NO X from Air,".
Mendoza, J.A., Lee, D.H., Kang, J.-H., 2016. Photocatalytic removal of NO x using TiO 2-coated zeolite. Environ. Eng. Res. 21 (3), 291–296.
Meng, L., Qu, Y., Jing, L., 2021. Recent advances in BiOBr-based photocatalysts for environmental remediation. Chin. Chem. Lett. 32 (11), 3265–3276.
Mera, A.C., Váldes, H., Jamett, F.J., Meléndrez, M., 2017. BiOBr microspheres for photocatalytic degradation of an anionic dye. Solid State Sci. 65, 15–21.
Mi, Y., Li, H., Zhang, Y., Du, N., Hou, W., 2018. Synthesis and photocatalytic activity of BiOBr nanosheets with tunable crystal facets and sizes. Catal. Sci. Technol. 8 (10), 2588–2597.
Mihaylov, M., et al., 2021. Infrared spectra of surface nitrates: revision of the current opinions based on the case study of ceria. J. Catal. 394, 245–258.
Milazzo, G., Caroli, S., Braun, R.D., 1978. Tables of standard electrode potentials. J. Electrochem. Soc. 125 (6), 261C.
Mills, A., Elouali, S., 2015. The nitric oxide ISO photocatalytic reactor system: measurement of NOx removal activity and capacity. J. Photochem. Photobiol. Chem. 305, 29–36.
Mills, A., Le Hunte, S., 1997. An overview of semiconductor photocatalysis. J. Photochem. Photobiol. Chem. 108 (1), 1–35.
Moeini, B., et al., 2022. Definition of a new (Doniach-Sunjic-Shirley) peak shape for fitting asymmetric signals applied to reduced graphene oxide/graphene oxide XPS spectra. Surf. Interface Anal. 54 (1), 67–77.
Montoya-Zamora, J., Martinez-De La Cruz, A., López-Cuéllar, E., González, F.P., 2020. BiOBr photocatalyst with high activity for NOx elimination. Adv. Powder Technol. 31 (8), 3618–3627.
Nargiello, M., Herz, T., 1993. Physical-chemical characteristics of P-25 making it extremely suited as the catalyst in photodegradation of organic compounds. Photocatalytic purification and treatment of water and air 3, 801–807.
O. World Health Organization and T. Environmental Health, 2006. "WHO Air quality guidelines for particulate matter, ozone, nitrogen dioxide and sulfur dioxide. Global Update 2005 : Summary of Risk Assessment,". World Health Organization, Geneva.
Organization, W.H., 2006. Air Quality Guidelines: Global Update 2005: Particulate Matter, Ozone, Nitrogen Dioxide, and Sulfur Dioxide. World Health Organization.
Patterson, A., 1939. The Scherrer formula for X-ray particle size determination. Phys. Rev. 56 (10), 978.
Prabhu, S.M., Pandi, K., Elanchezhiyan, S.S., Choi, J.-y., Kalaignan, G.P., Park, C.M., 2020. Ethylene glycol-induced metal alkoxides via phase-transfer catalyst as multi-talented adsorbents for boosted adsorption performance of toxic anions/oxyanions from waters. Separ. Purif. Technol. 235, 116247.
Qin, J., Zhao, R., Xia, M., 2020. A facile approach to synthesis carbon quantum dots-doped P25 visible-light driven photocatalyst with improved NO removal performance. Atmos. Pollut. Res. 11 (2), 303–309.
Quan, Y., YiO, M.H., Li, Y., Myers, R.J., Kafizas, A., 2023. Influence of Bi co-catalyst particle size on the photocatalytic activity of BiOI microflowers in Bi/BiOI junctions–A mechanistic study of charge carrier behaviour. J. Photochem. Photobiol. Chem. 443, 114889.
Sanchez, B., et al., 2021. NOx depolluting performance of photocatalytic materials in an urban area-Part II: assessment through Computational Fluid Dynamics simulations. Atmos. Environ. 246, 118091.
Shi, X., et al., 2019. Change in photocatalytic NO removal mechanisms of ultrathin BiOBr/BiOI via NO3–adsorption. Appl. Catal. B Environ. 243, 322–329.
Singh, S.P., Karmakar, B., 2010. Oxidative control of surface plasmon resonance of bismuth nanometal in bismuth glass nanocomposites. Mater. Chem. Phys. 119 (3), 355–358. https://doi.org/10.1016/j.matchemphys.2009.10.014.
Song, J.-M., Mao, C.-J., Niu, H.-L., Shen, Y.-H., Zhang, S.-Y., 2010. Hierarchical structured bismuth oxychlorides: self-assembly from nanoplates to nanoflowers via a solvothermal route and their photocatalytic properties. CrystEngComm 12 (11), 3875–3881.
Spicer, C.W., Kenny, D.V., Ward, G.F., Billick, I.H., 1993. Transformations, lifetimes, and sources of NO2, HONO, and HNO3 in indoor environments. Air Waste 43 (11), 1479–1485.
Sun, Y., et al., 2014. Growth of BiOBr nanosheets on C3N4 nanosheets to construct two-dimensional nanojunctions with enhanced photoreactivity for NO removal. J. Colloid Interface Sci. 418, 317–323.
Sun, Y., Zhao, Z., Dong, F., Zhang, W., 2015. Mechanism of visible light photocatalytic NO x oxidation with plasmonic Bi cocatalyst-enhanced (BiO) 2 CO 3 hierarchical microspheres. Phys. Chem. Chem. Phys. 17 (16), 10383–10390.
Sun, J., et al., 2023. Insight into the synergistic effect of metal surface plasmon resonance and clay loading to boost the antibiotics degradation of Bentonite/BiOBr/bismuth. Mater. Sci. Semicond. Process. 166, 107739.
Tan, X., Li, X., Yu, T., Zhao, Y., 2016. Preparation and photocatalytic activity of BiOBr/TiO2 heterojunction nanocomposites. Trans. Tianjin Univ. 22 (3), 211–217.
UNION, P., 2008. Directive 2008/50/EC of the European Parliament and of the Council of 21 May 2008 on Ambient Air Quality and Cleaner Air for Europe. Official Journal of the European Union.
Villabona-Leal, E., et al., 2020. Semiconducting polypyrrole@ TiO 2 pure anatase nanoparticles for photodegradation of reactive red 120 azo dye. J. Mater. Sci. Mater. Electron. 31, 12178–12190.
Wang, Y., Hong, B.H., Kim, K.S., 2005. Size control of semimetal bismuth nanoparticles and the UV− visible and IR absorption spectra. J. Phys. Chem. B 109 (15), 7067–7072.
Wang, Y., Deng, K., Zhang, L., 2011. Visible light photocatalysis of BiOI and its photocatalytic activity enhancement by in situ ionic liquid modification. J. Phys. Chem. C 115 (29), 14300–14308.
Wang, G., Xu, L., Zhang, J., Yin, T., Han, D., 2012. Enhanced photocatalytic activity of powders (P25) via calcination treatment. Int. J. Photoenergy 2012.
Wang, Y., Shi, Z., Fan, C., Wang, X., Hao, X., Chi, Y., 2013. Synthesis, characterization, and photocatalytic properties of BiOBr catalyst. J. Solid State Chem. 199, 224–229.
Wang, J., Zhang, Y., Tian, L., Liu, F., Xia, Q., 2014. Ultrathin BiOBr nanocrystals with dominant {001} facets and their high photocatalytic activity. J. Nanoparticle Res. 16, 1–10.
Wang, X.-j., et al., 2016. A chelation strategy for in-situ constructing surface oxygen vacancy on {001} facets exposed BiOBr nanosheets. Sci. Rep. 6 (1), 24918.
Wang, H., et al., 2018. Oxygen-vacancy-mediated exciton dissociation in BiOBr for boosting charge-carrier-involved molecular oxygen activation. J. Am. Chem. Soc. 140 (5), 1760–1766.
Wang, X., Zhang, F., Yang, Y., Zhang, Y., Liu, L., Lei, W., 2020. Controllable synthesis and photocatalytic activity of nano-BiOBr photocatalyst. J. Nanomater. 2020 (1), 1013075.
Wang, J., Fang, Y., Zhang, W., Yu, X., Wang, L., Zhang, Y., 2021. TiO2/BiOBr 2D-2D heterostructure via in-situ approach for enhanced visible-light photocatalytic N2 fixation. Appl. Surf. Sci. 567, 150623.
Watts, J.F., Wolstenholme, J., 2019. An Introduction to Surface Analysis by XPS and AES. John Wiley & Sons.
Wei, X.-X., Cui, H., Guo, S., Zhao, L., Li, W., 2013. Hybrid BiOBr–TiO2 nanocomposites with high visible light photocatalytic activity for water treatment. J. Hazard Mater. 263, 650–658.
Wu, X., et al., 2017. Improving the photo-oxidative capability of BiOBr via crystal facet engineering. J. Mater. Chem. A 5 (17), 8117–8124.
Xia, B., et al., 2022. TiO2/FePS3 S-scheme heterojunction for greatly raised photocatalytic hydrogen evolution. Adv. Energy Mater. 12 (46), 2201449.
Xin, Y., et al., 2023. Photocatalytic NO removal over defective Bi/BiOBr nanoflowers: the inhibition of toxic NO2 intermediate via high humidity. Appl. Catal. B Environ. 324, 122238.
Xu, F., Meng, K., Cheng, B., Wang, S., Xu, J., Yu, J., 2020. Unique S-scheme heterojunctions in self-assembled TiO2/CsPbBr3 hybrids for CO2 photoreduction. Nat. Commun. 11 (1), 4613.
Yagi, S., Tanaka, M., 1979. Mechanism of ozone generation in air-fed ozonisers. J. Phys. Appl. Phys. 12 (9), 1509.
Yu, H., et al., 2017. Liquid-phase exfoliation into monolayered BiOBr nanosheets for photocatalytic oxidation and reduction. ACS Sustain. Chem. Eng. 5 (11), 10499–10508.
Yu, F., Bai, X., Yang, C., Xu, L., Ma, J., 2019. Reduced graphene oxide–P25 nanocomposites as efficient photocatalysts for degradation of bisphenol a in water. Catalysts 9 (7), 607.
Yu, L., et al., 2023. Locally asymmetric BiOBr for efficient exciton dissociation and selective O2 activation toward oxidative coupling of amines. ACS Nano 17 (15), 15077–15084.
Zhang, G., Wang, X., 2013. A facile synthesis of covalent carbon nitride photocatalysts by Co-polymerization of urea and phenylurea for hydrogen evolution. J. Catal. 307, 246–253.
Zhang, X., Ai, Z., Jia, F., Zhang, L., 2008. Generalized one-pot synthesis, characterization, and photocatalytic activity of hierarchical BiOX (X= Cl, Br, I) nanoplate microspheres. J. Phys. Chem. C 112 (3), 747–753.
Zhang, D., Li, J., Wang, Q., Wu, Q., 2013. High {001} facets dominated BiOBr lamellas: facile hydrolysis preparation and selective visible-light photocatalytic activity. J. Mater. Chem. A 1 (30), 8622–8629.
Zhang, Y., et al., 2021. TiO2/BiOI pn junction-decorated carbon fibers as weavable photocatalyst with UV–vis photoresponsive for efficiently degrading various pollutants. Chem. Eng. J. 415, 129019.
Zhang, P., et al., 2021. Transformation of amorphous Bi2O3 to crystal Bi2O2CO3 on Bi nanospheres surface for photocatalytic NOx oxidation: intensified hot-electron transfer and reactive oxygen species generation. Chem. Eng. J. 420, 129814. https://doi.org/10.1016/j.cej.2021.129814.
Zhao, D., et al., 2008. Surface modification of TiO2 by phosphate: effect on photocatalytic activity and mechanism implication. J. Phys. Chem. C 112 (15), 5993–6001.
Zhao, W., et al., 2023. Construction of a TiO 2/BiOCl heterojunction for enhanced solar photocatalytic oxidation of nitric oxide. Dalton Trans. 52 (15), 4862–4872.
Zheng, M., Ma, X., Hu, J., Zhang, X., Li, D., Duan, W., 2020. Novel recyclable BiOBr/Fe 3 O 4/RGO composites with remarkable visible-light photocatalytic activity. RSC Adv. 10 (34), 19961–19973.
Zhong, J.B., et al., 2009. Characterization and photocatalytic property of Pd/TiO2 with the oxidation of gaseous benzene. J. Hazard Mater. 168 (2–3), 1632–1635.
Zhou, J., Takeuchi, M., Ray, A.K., Anpo, M., Zhao, X., 2007. Enhancement of photocatalytic activity of P25 TiO2 by vanadium-ion implantation under visible light irradiation. J. Colloid Interface Sci. 311 (2), 497–501.
Zhou, M., et al., 2015. Smog episodes, fine particulate pollution and mortality in China. Environ. Res. 136, 396–404.